

Stability Analysis of a Deterministic Dose Calculation for MRI-Guided Radiotherapy

by

Oleksandr Zelyak

A thesis submitted in partial fulfillment of the requirements for the degree of

Master of Science

in

Medical Physics

Department of Oncology
University of Alberta

© Oleksandr Zelyak, 2017

Abstract

Modern effort in radiotherapy to address the challenges of tumor localization and motion has led to the development of MRI guided radiotherapy technologies. Accurate dose calculations must properly account for the effects of the MRI magnetic fields. St-Aubin et al. (2015, 2016) have investigated the accuracy of a deterministic linear Boltzmann transport equation (LBTE) solver that includes magnetic field, but not the stability of the iterative solution method. This thesis performs a stability analysis of this deterministic algorithm including an investigation of the convergence rate dependencies on the magnetic field, material density, energy, and anisotropy expansion. The iterative convergence rate of the continuous and discretized LBTE including magnetic fields is determined by analyzing the spectral radius using Fourier analysis for the stationary source iteration (SI) scheme. The spectral radius is calculated when the magnetic field is included 1) as a part of the iteration source, and 2) inside the streaming-collision operator. The non-stationary Krylov subspace solver GMRES is also investigated as a potential method to accelerate the iterative convergence, and an angular parallel computing methodology is investigated as a method to enhance the efficiency of the calculation. SI is found to be unstable when the magnetic field is part of the iteration source, but unconditionally stable when the magnetic field is included

in the streaming-collision operator. The discretized LBTE with magnetic fields using a space-angle upwind stabilized discontinuous finite element method (DFEM) was also found to be unconditionally stable, but the spectral radius rapidly reaches unity for very low-density media and increasing magnetic field strengths indicating arbitrarily slow convergence rates. However, GMRES is shown to significantly accelerate the DFEM convergence rate displaying only a weak dependence on the magnetic field. In addition, the use of an angular parallel computing strategy is shown to potentially increase the efficiency of the dose calculation.

Keywords: linear Boltzmann transport equation, magnetic field, dose calculation, MRI guided radiotherapy, finite element analysis, GMRES, stability analysis

Acknowledgments

I would like to thank my supervisors Dr. St-Aubin, Dr. Fallone, and my friend Ray Yang for their great support, guidance and encouragement. I also would like to thank Alberta Cancer Foundation (Antoine Noujaim entrance scholarship) and the Alberta Innovates Health Solutions (CRIO TEAM grant 2016006) for provided financial support.

Contents

Abstract	ii
Acknowledgments	iv
List of Figures	vii
1 Introduction	1
1.1 Radiotherapy Dose Calculations	1
1.2 Magnetic Resonance Imaging (MRI) Guided Radiotherapy (RT) Technologies	6
1.3 Thesis Motivation	9
1.4 Thesis Outline	10
2 Methods	13
2.1 Linear Boltzmann Transport Equation	13
2.2 Stationary Iterative Schemes	24
2.2.1 Overview of Stationary Iterative Solvers	24
2.2.2 Source Iteration	29
2.3 Fourier Analysis Method	30

2.4	Multigroup Method	33
2.5	Discrete Ordinates Method	36
2.6	Finite Element Method	39
2.6.1	Angular Domain Discretization	50
2.6.2	Spatial Domain Discretization	53
2.6.3	Discontinuous Galerkin Finite Element Method	56
3	Analysis of the Spectral Radius in an Infinite Medium — Continuous LBTE	61
3.1	Continuous LBTE with no Magnetic Fields	61
3.2	Continuous LBTE with Magnetic Fields	71
4	Spectral Radius of the Discretized Equations in Infinite Medium	80
5	Improving the Convergence Rate via an Efficient Krylov-Subspace Solver	92
6	Conclusion and Future Work	99
	Bibliography	105

List of Figures

2.1	The element of infinitesimal physical volume dV	15
2.2	Representation of the discretization of the energy variable.	34
2.3	Orthogonality of approximate solution and solution error.	43
2.4	Piecewise linear approximation $\tilde{u}(x)$ of the solution $u(x)$	47
2.5	Hat-shaped basis functions used in linear piecewise approximation. . .	48
2.6	An example tessellation of the angular domain on the unit sphere. This tessellation contains 512 elements.	50
2.7	A 40 element tessellation is unwrapped onto a flat 2D surface with some points added at the poles $\theta = 0, \pi$	51
2.8	Basis functions $\gamma_i^p(\varphi, \theta)$ represent pieces of 2D plane in 3D and acquire unity at node i and zero at opposite side of triangle.	53
2.9	Partition of L^3 cube into spatial 3D finite elements.	54
3.1	Spectral radius as a function of magnetic field parameter as predicted by Eq. (3.52) (solid line), and extracted numerically according to Eq. (2.55) using previously published code (St-Aubin et al., 2016). . .	75

3.2	(a) Eigenvalue modulus ($ \omega $) for various magnetic field parameter values inside $m = 1$ block of iteration matrix T in Eq. (3.62) as a function of the Fourier wave number λ , and (b) eigenvalue modulus as a function of the Fourier wave number λ and block number m for the fixed magnetic field parameter value $\kappa B = 10 \text{ cm}^{-1}$	78
4.1	The Henyey-Greenstein function is used to model differential scattering cross section $\sigma_s(\vec{\Omega} \cdot \vec{\Omega}')$ for two values of anisotropy parameter $g = 0$ and 0.7	82
4.2	Angular finite element mesh showing the direction of the magnetic field operator $\vec{\tau}$ and sweeping direction (arrows).	85
4.3	Spatial domain (cube) partitioned into six tetrahedrons. The main domain (solid lines) is periodically translated (dashed lines) to simulate an infinite medium.	86
4.4	Spectral radius as a function of the magnetic field parameter for several medium densities with $c = 0.2$. Details of implementation of published code can be found in (St-Aubin et al., 2016).	90
5.1	Eigenvalue spectrum of the matrix \mathbf{A} for various magnetic field parameter strengths. As the magnetic field parameter increases, the eigenvalues tend to cluster closer to zero, which is expected to have a negative impact on the convergence rate of GMRES.	95
5.2	Comparison of the effectiveness of GMRES and SI iterative methods. [Curve #1: $g = 0, c = 0.2, \sigma = 10^{-3} \text{ cm}^{-1}$], [Curve #2: $g = 0.7, c = 0.2, \sigma = 10^{-3} \text{ cm}^{-1}$], [Curve #3: $g = 0.7, c = 0.99, \sigma = 10^3 \text{ cm}^{-1}$].	97

6.1	(a) Example of grid slab partitioning in the angular domain. Each slab is presumed to be solved in parallel independently, and (b) dependence of the relative number of GMRES iterations on the degree of parallelization.	103
-----	--	-----

Chapter 1

Introduction

1.1 Radiotherapy Dose Calculations

Dose calculation algorithms are an essential part of successful treatments in radiation therapy. Absorbed dose is a parameter that allows for the estimation of the effectiveness of a prescribed treatment. The development of dose calculation methodologies has a long history beginning in the 1950s. Due to the growing knowledge about the interaction of radiation with matter, and the rapid development of computational capabilities, dose calculations have progressed from basic correction-based methods (Clarkson, 1941; Cunningham, 1972; Khan et al., 1973), up to advanced Monte Carlo (Fippel, 2013) and deterministic methods (Lewis and Miller, 1993; Vassiliev et al., 2010). Two essential requirements for 3D radiotherapy dose calculations are 1) a high degree of accuracy and, 2) low calculation times for rapid transitions from treatment planning to treatment. Accuracy is required to be able to correlate tumor responses

in a patient with a delivered dose for a better understanding the biological response mechanisms in radiotherapy, and to predict future outcomes. Fast calculation speeds ensure that treatment planning is completed within a reasonable time span that does not disrupt the clinical flow.

All radiotherapy treatment planning algorithms aim to solve or approximate the solution to the integro-differential linear Boltzmann transport equation (LBTE) which describes radiation interaction with matter. Despite the linearity, the LBTE is a complex equation and is challenging to solve in general. Its solution provides a macroscopic description of the propagation of ionization radiation in matter by specifying the position and momentum probability distribution of a radiation field. As many different particles generally make up a full radiation field (e.g. photons, electrons, positrons, etc.), a full description is obtained from the solution of a system of coupled integro-differential LBTE equations. In this manner each equation describes the interaction process for a given particle which is then coupled to the equations of other particle types by through the process of secondary particle generation (Lewis and Miller, 1993).

Existing dose calculation methods can be divided into three categories based on their approach to solve the coupled LBTE equations; correction-based, model-based, and principle-based algorithms (Lu, 2013). The first methods employed in radiotherapy planning were empirical correction-based algorithms. These methods were developed under the assumption that patients are essentially water and radiation dose deposition in patients can be described by radiation ionizations in a homogeneous water medium (Schoknecht, 1967). Dose determination to a point was obtained by means of dose functions (e.g. percent depth dose, tissue-phantom ratio, etc.) obtained via

direct measurements in a water phantom (Clarkson, 1941; Cunningham, 1972; Khan et al., 1973). To account for changes based on tissue inhomogeneities, various correction algorithms are applied (Ahnesjö and Aspradakis, 1999; Batho, 1964; Sontag and Cunningham, 1978). For example, the simplest method is the equivalent path length method, that uses a multiplicative correction factor to a water based calculation. The correction factor is the ratio of tissue air ratio (TAR) or tissue phantom ratio (TPR) dose functions, where the depth to a calculation point is replaced by effective (radiological) depth equal to the thickness of water-equivalent tissue that would attenuate the radiation by the same amount. This method does not account for the size and the distance to an inhomogeneity. To account for position of the inhomogeneity, the power-law correction (Batho correction) is used. The correction factor, which is the ratio of TAR (or TPR) dose functions, is raised to a power that depends on the electronic density of surrounding material. To account for 3D shape of the inhomogeneity, an equivalent tissue air ratio (ETAR) correction can be used. This correction was developed by Sontag and Cunningham (1978) who proposed that in the correction factor of the ratio of TAR dose functions, both the depth and the size of the field at calculation point be appropriately scaled.

The advantage of these methods is their simplicity and speed. On the other hand, these early correction-based algorithms do not provide 3D dose information, and in complex cases of heterogeneous media, these methods can produce significant error due to an inability to account for lateral scattering (Papanikolaou, 2004).

The next level of sophistication is achieved in model-based algorithms, also known as convolution/superposition algorithms (Ahnesjö, 1989; Mackie et al., 1985; Oelkfe and Scholz, 2006). In their dose calculation, these models explicitly consider macro-

scopic physical processes of energy deposition within a patient. This is done by introducing various dose kernels – the distribution functions that describe energy transport and dose deposition originating from photon-tissue interactions. The dose kernels are usually derived from more accurate Monte Carlo simulations.

Convolution/superposition algorithms, which can provide a 3D dose distribution, simulate the dose deposition in several stages. The initial stage requires a model of the radiation field emerging from a medical linear accelerator. This radiation field serves as an input for the next stage, where the absorption of primary photons in a patient is quantified in terms of the total energy released per unit mass (TERMA), (Ahnesjö et al., 1987). Finally, dose kernels are used to simulate the process of electron energy transport and deposition based on the calculated TERMA.

One type of dose kernel often used in calculations is the point-spread kernel. It describes the distribution of energy in a medium if it was released locally at specific point due to the interaction of primary photons of energy E . The 3D dose distribution is calculated by superposition of TERMA volume with energy deposition kernel. The total dose in the patient is calculated by adding the contribution of all point-spread kernels in the target region.

Computational load is significantly reduced in the case of a homogeneous medium where point-spread kernel becomes translationally invariant (Oelkfe and Scholz, 2006).

Physically the most rigorous 3D dose calculations are principle-based methods which include stochastic Monte Carlo methods as well as deterministic methods that directly solve the integro-partial differential LBTE. These particle transport based methods can be used for problems of practically any complexity appearing in clinical

RT practice.

Monte Carlo is a stochastic approach based on tracing the individual tracks of primary and secondary particles as they propagate and interact with matter via fundamental physical processes (Fippel, 2013). Each type of interaction is modeled by a random sampling of cross section distributions attributed to a particular interaction. Similar to the model-based methods, Monte Carlo also requires a model of radiation field emerging from linear accelerator, typically stored as a six-dimensional particle phase space describing the particle momentum and position.

The uncertainty of Monte Carlo simulations depends on the inverse square root of the number of particle histories (Jeraj and Keall, 2000). This typically makes Monte Carlo simulations rather time consuming as a very large number of histories is required to be calculated. However, recent advances in Graphics Processing Unit (GPU) and Central Processing Unit (CPU) computing, and the application of various radiotherapy specific assumptions and acceleration techniques have significantly reduced Monte Carlo dose calculation time (Hissoiny et al., 2011). This makes Monte Carlo feasible for use in clinical treatment planning systems such as the XVMC algorithm used in the Elekta Monaco treatment planning system (Fippel, 1999). Due to its high accuracy, validated through comparison with experimental measurements, Monte Carlo algorithms are also often used for benchmarking the accuracy of other dose calculation algorithms (Tertel et al., 2010).

As opposed to stochastic algorithms, deterministic methods, also known as grid-based Boltzmann solvers (Vassiliev et al., 2010), calculate the dose distribution by solving a system of linear equations obtained by discretizing the six-dimensional phase

space variables of the LBTE. The six-dimensional phase space variables (typically space, angle and energy) can be discretized using various techniques including finite element methods, discrete ordinates methods, and Multigroup methods (Gifford et al., 2006; Lewis and Miller, 1993). Acuros XB is a principle-based grid-based Boltzmann solver developed by Varian Medical Systems which has been shown to have equivalent accuracy to Monte Carlo calculations for external photon beam treatment planning in complex heterogeneous cases (Failla et al., 2010; Han et al., 2011). Acuros XB explicitly solves the LBTE with accuracy comparable to advanced Monte Carlo methods. In fact, Acuros XB was developed as a faster alternative to Monte Carlo methods (Failla et al., 2010).

1.2 Magnetic Resonance Imaging (MRI) Guided Radiotherapy (RT) Technologies

Modern efforts in radiotherapy to address the challenges of tumor localization while sparing radiation sensitive organs has led to the development of magnetic resonance imaging (MRI) guided radiotherapy (RT) technologies. MRI-guided RT systems add a requirement that magnetic fields be properly accounted for in the dose calculations. In radiotherapy, the dose to a tumor that kills cancer cells is deposited by a flux of charged particles (primary or secondary) such as electrons, protons, carbon ions, etc. The presence of the magnetic field alters primary and secondary charged particle trajectories due to the Lorentz force and influences the final dose distribution. The magnitude of the effect in the final dose depends on a set of parameters including the MRI magnetic field strength, tissue density and mutual orientation of the MRI field

and radiation beam.

The main dose effects observed in simulations and experiments for magnetic fields perpendicular to the radiation beam include the reduction of build-up (surface) dose, asymmetry of lateral profile perpendicular to the magnetic field and dose increase at tissue-air interfaces due to returning electrons (Raaijmakers et al., 2005, 2007). In strong parallel magnetic fields lateral confinement of secondary electrons is observed which can be used to increase the dose delivered to a tumor (Bielajew, 1993; Kirkby et al., 2010). It also increases the skin dose due to confinement of contaminant electrons (Keyvanloo et al., 2016).

There are currently several MRI-guided RT systems that have the capacity to be used in the clinical environment. One of the first MRI-guided RT projects began at the Cross Cancer Institute in Edmonton Alberta, Canada by coupling a 6 MV linear accelerator to a bi-planar MRI. In 2008, the Alberta group demonstrated the first simultaneous MR imaging and linac irradiation on head-size phantoms (Fallone et al., 2009). In 2013, the Alberta group began installing a whole body 0.5 T high temperature superconducting bi-planar MRI coupled to a 6 MV linac¹. The world's first images of a human volunteer were obtained on this system in July 2014¹. In this linac MR system the magnetic field is parallel to the radiation beam. Lateral confinement of electrons in the parallel magnetic field helps avoid significant dose increase at tissue-air interfaces inside the patient and at beam exit. The lower strength of the magnetic field allows for the usage of a cryogen-free high temperature superconducting magnet which reduces the overall cost of radiation vault design and installation. On the other hand, the lower magnetic field results in lower signal-to-noise ratio (SNR)

¹Linac-MRI records first human images: <http://medicalphysicsweb.org/cws/article/opinion/58572>

of the MRI images.

Elekta has also developed the Unity MR-linac platform using a 7 MV linac source coupled to a 1.5 T superconducting solenoid MRI (Raaymakers et al., 2009). The high magnetic field strength allows better quality MRI images. This platform utilizes geometry where the radiation beam is perpendicular to the magnetic field. This reduces the entrance dose due to contaminant electrons, but creates large dose perturbation caused by electron return effect at tissue-air and tissue-lung interfaces (Kirkby et al., 2010).

The first commercial MRI-guided RT system (MRIdian™) was developed by ViewRay Inc., which coupled three radioactive ^{60}Co sources to a 0.35 T split solenoid MRI (Dempsey et al., 2005). It is the first MRI RT system to clinically treat patients. The SNR of this system is also reduced due to the lower magnetic field strength. The use of ^{60}Co sources provides lower mean energy of 1.25 MV, and was initially used to avoid radiofrequency (RF) and magnetic coupling between the linac and MRI. However, it was shown previously that the linac and MRI can be magnetically and RF decoupled quite simply (Santos et al., 2012; St-Aubin et al., 2010). The quality of IMRT treatment plans produced by ViewRay MR-guided radiotherapy system was assessed by the scientists from Washington University School of Medicine, St. Louis, Missouri (Wooten et al., 2015). Although additional tests are still in progress, the group concluded that the ^{60}Co MR-IGRT device can prepare IMRT treatment plans comparable in quality to linac IMRT for various disease sites. Currently, ViewRay is developing a new linac based MRI-guided RT system (Low et al., 2016) with 6 MV linac and the 0.35 T MRI technology.

1.3 Thesis Motivation

Historically, Monte Carlo was the only option to include the effects of magnetic fields in the calculation of absorbed dose. The MRIdianTM radiation therapy system from ViewRay Inc. developed a commercial Monte Carlo based algorithm which incorporates the effect of magnetic fields on charged particle transport (<http://www.viewray.com/treatment>), as did Elekta with GPUMCD in the Monaco treatment planning system (Hissoiny et al., 2011).

However, in addition to traditional Monte Carlo methods, it was shown recently that grid-based Boltzmann solvers were capable of accurately incorporating magnetic fields into a deterministic solution of the LBTE (St-Aubin et al., 2015, 2016). In the 2015 publication by St-Aubin et al., very accurate results were shown comparing deterministic dose calculations in magnetic fields to Monte Carlo calculations, but it was stated that the iterative solution method used, coupled with the discretization method, produced an unstable iterative scheme in low density media with magnetic fields. In 2016, St-Aubin published a space-angle discontinuous finite element discretization with magnetic fields that was shown to alleviate the iterative instability of the 2015 work (St-Aubin et al., 2016). The motivation for this work stems from the fact that a rigorous iterative stability analysis for these novel methods including magnetic fields has not been presented. In this work, a Fourier stability analysis is performed to rigorously determine the iterative stability of the numerical approaches presented by St-Aubin et al. (2015, 2016).

1.4 Thesis Outline

The structure of this thesis is as follows. Chapter **2** introduces many of the important theoretical definitions required for this thesis. It starts with the theoretical background of the LBTE including magnetic fields followed by an outline of the theory of iterative methods for solving systems of linear equations in general. The source iteration method specifically discusses as it is often applied to solve the linear Boltzmann transport equation and is used in the methods presented by St-Aubin et al. (2016). The Fourier analysis method, central to this work, is then presented as a method to calculate the spectral radius of the iterative solution. As explained in this chapter, the spectral radius is the key metric to determine whether or not a stationary iterative scheme, such as source iteration, is stable. A thorough description of the various discretization techniques is then described beginning with the multigroup method for the energy discretization. Discrete ordinate method is then described as a means of discretization of angular variable, and serves as a prelude to the more suitable angular discretization by the Finite Element Method (FEM) for the LBTE in the presence of magnetic fields. The necessary theoretical basis of the FEM is thus presented for both spatial and angular variables. Finally, application of the Discontinuous Finite Element Method (DFEM) to the LBTE in the presence of magnetic fields is presented.

Chapter **3** uses the theoretical foundation built in chapter **2** to apply the Fourier analysis method to the continuous LBTE in infinite medium as a means of calculating the spectral radius. The calculations begin with analysis of the LBTE with no magnetic fields to serve as a benchmark. Then, the spectral radius is extracted for

two situations of interest where magnetic field operator is a part of iteration source on the right side of the equation, and when it is a part of the streaming-collision operator on the left side. The detailed analysis of the dependence of the spectral radius on various system parameters such as magnetic field strength, material density and degree of anisotropy is provided.

In chapter **4** furthers the analysis presented in chapter **3** by calculating the spectral radius for the DFEM discretized LBTE. In particular, the effects of anisotropy are studied using the Heyhey-Greenstein model for electron differential cross sections. Different regimes of scattering and material density are controlled by varying the scattering ratio and total cross section. The dependence of the spectral radius on the magnetic field is revealed and the necessity of more advanced solver than the stationary source iteration scheme is stressed.

To overcome the slow convergence issues related to source iteration of the discretized LBTE with magnetic fields, chapter **5** introduces the non-stationary Krylov subspace method (GMRES) as an alternative. This method is applied to estimate the convergence properties of the solution of LBTE in homogeneous medium vs magnetic field based on the eigenvalue dynamics of Krylov the operator. The efficiency of GMRES is numerically quantified based on the number of iterations required to achieve a prescribed accuracy. This efficiency is compared with the source iteration method.

As an additional method to speed up calculations, a methodology of parallel computing in angular domain is partially described in chapter **6** as a part of future work. This method complements the benefits of the Krylov subspace solver GMRES pre-

sented in chapter **5**. A semi quantitative explanation of the conditions for efficient parallelization is presented followed by the result of the simulations for different degrees of parallelization.

Chapter **6** concludes the thesis with the reciting of this work's objectives, a condensed description of obtained results, and potential future work.

Chapter 2

Methods

2.1 Linear Boltzmann Transport Equation

This chapter begins with the derivation of the Linear Boltzmann Transport Equation. The derivation is along the lines presented in (Lewis and Miller, 1993). Even though the equation is derived with the electron transport in mind, this approach is quite general and can be applied to neutral particles transport (photons, neutrons) or other charged particles (positrons, protons, etc.).

As many fundamental equations of mathematical physics, the LBTE is a consequence of particle conservation. The dynamics of one particle is described by its time dependent position \vec{r} and velocity \vec{v} . Alternatively, it can be described in terms of spatial position \vec{r} , direction of propagation $\vec{\Omega} = \vec{v}/v$, and energy E . A transport equation is usually formulated for a quantity that describes a macroscopic picture from the motion for many particles. Let's first consider a *particle density distribution*

$N(\vec{r}, \vec{\Omega}, E, t)$. This function depends on seven independent variables: space, angle, energy and time. For an infinitesimally small spatial volume dV with its center at \vec{r} , it physically denotes the number of particles at time t propagating in the direction $\vec{\Omega}$ within the solid angle $d\Omega$ with energy inside the interval dE around E ,

$$dN(\vec{r}, \vec{\Omega}, E, t) = N(\vec{r}, \vec{\Omega}, E, t) dV dE d\Omega. \quad (2.1)$$

The density distribution $N(\vec{r}, \vec{\Omega}, E, t)$ is a fundamental dependent variable which can be used to derive other dependent variables. In radiation transport, a more convenient dependent variable is an angular flux $\psi(\vec{r}, \vec{\Omega}, E, t)$,

$$\psi(\vec{r}, \vec{\Omega}, E, t) \equiv vN(\vec{r}, \vec{\Omega}, E, t) \quad (2.2)$$

where v is the particle speed. A transport equation can be found by considering the processes leading to the change in the total number of particles inside dV . For our purposes we focus on the following: (a) streaming of particles across the boundary of volume dV , (b) collisions inside dV that send particles outside the interval dE around energy E and outside the solid angle $d\Omega$ around direction $\vec{\Omega}$, (c) collisions inside dV that scatter particles with energy E' and direction $\vec{\Omega}'$ into the energy interval dE around E , and into the solid angle $d\Omega$ along $\vec{\Omega}$, and (d) a source of particles inside dV with energy E in the direction $\vec{\Omega}$.

Consider the streaming of particles through the physical volume dV . Since all the particles travel in the same direction, it is convenient to choose the shape of dV symmetric with respect to $\vec{\Omega}$, for example a cylindrical shape of $dV = dA du$ as shown in Fig. (2.1), where dA and du are the area of the ends and the height of the cylinder.

For this shape of dV we can be sure that particles cross only the ends of the cylinder, but not its sides. The change of dN in dV due to streaming is equal to the difference

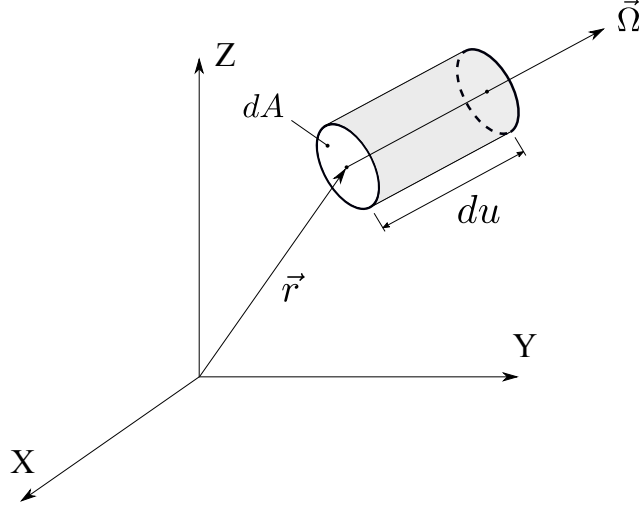


Figure 2.1: The element of infinitesimal physical volume dV .

in the number of particles entering dV at \vec{r} and leaving dV at $\vec{r} + d\vec{u}$,

$$\left[N(\vec{r} + d\vec{u}, \vec{\Omega}, E, t) - N(\vec{r}, \vec{\Omega}, E, t) \right] dA v dt dE d\Omega. \quad (2.3)$$

Due to the small values of $d\Omega$ and dE it is assumed that even one collision is enough for a particle to acquire a different energy E' and/or move in a different direction $d\vec{\Omega}'$ so it contributes to a decrease in particle density dN . To find the number of such particles we use a probabilistic interpretation of total cross section $\sigma(\vec{r}, E)$ (Lewis and Miller, 1993) as the probability for a particle to experience a collision per unit path length. The total distance traversed by all particles in dV with energy E along $\vec{\Omega}$ is $N(\vec{r}, \vec{\Omega}, E, t) dA du dE d\Omega v dt$. Then, the total number of collisions contributing to change in dN is

$$\sigma(\vec{r}, E) v N(\vec{r}, \vec{\Omega}, E, t) dA du dE d\Omega dt. \quad (2.4)$$

There is an opposite process when a particle inside dV with energy E' propagating in direction $\vec{\Omega}'$ scatters into the state with $(E, \vec{\Omega})$ after a collision. This process increases the value of the particle density dN . Like the total cross section, the differential cross section $\sigma_s(\vec{r}, E' \rightarrow E, \vec{\Omega}' \cdot \vec{\Omega}) dE d\Omega$ is a probability per unit path length for a particle to scatter from state $(E', \vec{\Omega}')$ to $(E, \vec{\Omega})$. The angular dependence $\vec{\Omega}' \cdot \vec{\Omega}$ means that scattering potential depends only on the mutual orientation of $\vec{\Omega}$ and $\vec{\Omega}'$. Using this definition for differential cross section, the total number of particles inside dV that scatter into state $(E, \vec{\Omega})$ is

$$\left[\int_0^\infty dE' \int d\Omega' \sigma_s(\vec{r}, E' \rightarrow E, \vec{\Omega}' \cdot \vec{\Omega}) v N(\vec{r}, \vec{\Omega}', E', t) \right] dA du dE d\Omega dt. \quad (2.5)$$

Another term, contributing to the increase of particle density, is due to a source and can be written as

$$S(\vec{r}, \vec{\Omega}, E, t) du dA dE d\Omega dt. \quad (2.6)$$

Finally, the total change in density distribution dN over time dt is

$$dN(\vec{r}, \vec{\Omega}, E, t + dt) - dN(\vec{r}, \vec{\Omega}, E, t) = \left[N(\vec{r}, \vec{\Omega}, E, t + dt) - N(\vec{r}, \vec{\Omega}, E, t) \right] du dA dE d\Omega. \quad (2.7)$$

The total change in dN with time is a result of all the processes described by

Eqs. (2.3 – 2.6)

$$\begin{aligned}
& \left[N(\vec{r}, \vec{\Omega}, E, t + dt) - N(\vec{r}, \vec{\Omega}, E, t) \right] du dA dE d\Omega = - \left[vN(\vec{r} + d\vec{u}, \vec{\Omega}, E, t) \right. \\
& \quad \left. - vN(\vec{r}, \vec{\Omega}, E, t) \right] dA dE d\Omega dt - \sigma(\vec{r}, E) vN(\vec{r}, \vec{\Omega}, E, t) du dA dE d\Omega dt \\
& \quad + \left[\int_0^\infty dE' \int d\Omega' \sigma_s(\vec{r}, E' \rightarrow E, \vec{\Omega}' \cdot \vec{\Omega}) vN(\vec{r}, \vec{\Omega}', E', t) \right] du dA dE d\Omega dt \\
& \quad + S(\vec{r}, \vec{\Omega}, E, t) du dA dE d\Omega dt. \tag{2.8}
\end{aligned}$$

The transport equation for the angular flux $\psi = vN(\vec{r}, \vec{\Omega}, E, t)$ is obtained from Eq. (2.8) by dividing left and right sides by $du dA dE d\Omega dt$,

$$\begin{aligned}
\frac{d\psi(\vec{r}, \vec{\Omega}, E, t)}{dt} &= - \left[\vec{\Omega} \cdot \vec{\nabla}_r + \sigma(\vec{r}, E) \right] \psi(\vec{r}, \vec{\Omega}, E, t) \\
& \quad + \int_0^\infty dE' \int d\Omega' \sigma_s(\vec{r}, E' \rightarrow E, \vec{\Omega}' \cdot \vec{\Omega}) \psi(\vec{r}, \vec{\Omega}', E', t) + S(\vec{r}, \vec{\Omega}, E, t). \tag{2.9}
\end{aligned}$$

For stationary problems the total time derivative is zero, and time independent LBTE is written as

$$\begin{aligned}
\left[\vec{\Omega} \cdot \vec{\nabla}_r + \sigma(\vec{r}, E) \right] \psi(\vec{r}, \vec{\Omega}, E) &= \\
& \quad \int_0^\infty dE' \int d\Omega' \sigma_s(\vec{r}, E' \rightarrow E, \vec{\Omega}' \cdot \vec{\Omega}) \psi(\vec{r}, \vec{\Omega}', E') + S(\vec{r}, \vec{\Omega}, E). \tag{2.10}
\end{aligned}$$

To provide a description of the full radiation field, we need to express Eq. (2.10) for photons, electrons, and positrons. This full description will include the coupling

between each of the particle types through the generation of secondary particles.

$$\left[\vec{\Omega} \cdot \vec{\nabla}_r + \sigma^\gamma(\vec{r}, E) \right] \psi_\gamma(\vec{r}, \vec{\Omega}, E) = Q^{\gamma\gamma} + Q^{p\gamma} + Q^{e\gamma} + S_\gamma \quad (2.11)$$

$$\left[\vec{\Omega} \cdot \vec{\nabla}_r + \sigma^e(\vec{r}, E) \right] \psi_e(\vec{r}, \vec{\Omega}, E) = Q^{ee} + Q^{\gamma e} + Q^{pe} + S_e \quad (2.12)$$

$$\left[\vec{\Omega} \cdot \vec{\nabla}_r + \sigma^p(\vec{r}, E) \right] \psi_p(\vec{r}, \vec{\Omega}, E) = Q^{pp} + Q^{\gamma p} + Q^{ep} + S_p. \quad (2.13)$$

where indices γ , e , and p denote photons, electrons and positrons respectively.

The generic form of the scattering integral Q^{xy} has the form,

$$Q^{xy} = \int_0^\infty dE' \int d\Omega' \sigma_s^{xy}(\vec{r}, E' \rightarrow E, \vec{\Omega}' \cdot \vec{\Omega}) \psi_x(\vec{r}, \vec{\Omega}', E'). \quad (2.14)$$

The differential scattering cross section σ_s^{xy} is the probability per unit path length for a particle of type x to create a particle of type y , and ψ_x is the angular fluence of particle of type x .

The common approximation in radiotherapy calculations is to treat positrons on the same footing as electrons. This effectively removes the equation for positron fluence. Another important approximation is that there is no Bremsstrahlung production of photons by electrons. Therefore, $\sigma_s^{e\gamma}$ is set to zero. It is assumed that all the energy due to Bremsstrahlung radiation is deposited locally. This assumption enormously simplifies the dose calculations without affecting the final result since the probability of Bremsstrahlung and annihilation photon production in the clinical range of electron energies is very small (Gifford et al., 2006).

With this approximations, the systems of Eqs. (2.11–2.13) is reduced to the

following system,

$$\left[\vec{\Omega} \cdot \vec{\nabla}_r + \sigma^\gamma(\vec{r}, E) \right] \psi_\gamma(\vec{r}, \vec{\Omega}, E) = Q^{\gamma\gamma} + S_\gamma \quad (2.15)$$

$$\left[\vec{\Omega} \cdot \vec{\nabla}_r + \sigma^e(\vec{r}, E) \right] \psi_e(\vec{r}, \vec{\Omega}, E) = Q^{ee} + Q^{\gamma e} + S_e. \quad (2.16)$$

The deposited dose is calculated as

$$D(\vec{r}) = \int dE \int d\Omega \frac{\sigma_{ED}(\vec{r}, E)}{\rho} \psi_e(\vec{r}, E, \vec{\Omega}), \quad (2.17)$$

where, σ_{ED} is the energy deposition cross section, and ρ is the density of the material.

We will be dealing with slightly modified version of the electron transport Eq.(**2.16**). For convenience, we drop sub-index e for electron fluence ψ_e and electron source S_e (assuming that $\psi_e = \psi$ and $S_e = S$). In a clinical range of energies, secondary electron deposits its energy predominantly by interacting with the electrons of the medium. The result of these interactions is the loss of the electron's energy and change in the direction of propagation. The majority of interactions are soft collisions (as opposed to hard collisions) and result only in a small energy change. To facilitate the calculations, the soft collisions are separated from the hard collisions in the electron-electron collisional integral Q^{ee} in Eq. (**2.16**). For this reason, the integration over energy in Q^{ee} is split into two integrals, one of which describes hard collisions, and the other takes into account soft collisions.

Morel applied the Fokker-Planck approximation to the soft collisions of Q^{ee} (Morel, 1981) and showed that this part of the collisional integral can be represented by a

simpler expression of the form

$$\int_0^\infty dE' \int d\Omega' \sigma_s^{ee}(\vec{r}, E' \rightarrow E, \vec{\Omega}' \cdot \vec{\Omega}) \psi(\vec{r}, \vec{\Omega}', E') \approx \frac{\alpha}{2} \frac{\partial}{\partial \mu} \left((1 - \mu^2) \frac{\partial}{\partial \mu} \psi(\vec{r}, \vec{\Omega}, E) \right) + \frac{\partial}{\partial E} \left(\beta_r(\vec{r}, E) \psi(\vec{r}, \vec{\Omega}, E) \right) + \frac{1}{2} \frac{\partial^2}{\partial E^2} \left(\gamma_r(\vec{r}, E) \psi(\vec{r}, \vec{\Omega}, E) \right) \quad (2.18)$$

This type of approximation is used whenever the majority of the scattering processes result in a small energy loss and/or small scattering angle. Small energy loss or small deviation in angle serve as parameters for a Taylor expansion of the integral Boltzmann scattering operator.

The coefficients α , β_r , and γ_r are the momentum transfer, restricted mass stopping power, and restricted mean-square stopping power respectively. In an external beam photon radiotherapy case, the coefficients α and γ_r are approximated as zero with almost negligible error to the final solution (Gifford et al., 2006). In this approximation, the soft collisions electron-electron scattering integral becomes

$$\int_0^\infty dE' \int d\Omega' \sigma_{s,soft}^{ee}(\vec{r}, E' \rightarrow E, \vec{\Omega}' \cdot \vec{\Omega}) \psi(\vec{r}, \vec{\Omega}', E') \approx \frac{\partial}{\partial E} \left(\beta_r(\vec{r}, E) \psi(\vec{r}, \vec{\Omega}, E) \right). \quad (2.19)$$

The mass stopping power β_r is defined as the ratio of energy dE_c lost due to collisions with other electrons over the distance dl , divided by the density of the medium ρ . The energy transferred to other electrons of the medium is restricted by Δ ; that is, $dE_c \leq \Delta$. The term on the right-hand side of Eq. (2.19) is called continuous slowing down (CSD) operator, and Boltzmann equation containing this

term is called CSD linear Boltzmann transport equation, or CSD-LBTE,

$$\left[\vec{\Omega} \cdot \vec{\nabla}_r + \sigma(\vec{r}, E) \right] \psi(\vec{r}, \vec{\Omega}, E) - \frac{\partial}{\partial E} \left(\beta_r(\vec{r}, E) \psi(\vec{r}, \vec{\Omega}, E) \right) = \int_0^\infty dE' \int d\Omega' \sigma_s^{ee}(\vec{r}, E' \rightarrow E, \vec{\Omega}' \cdot \vec{\Omega}) \psi(\vec{r}, \vec{\Omega}', E') + S(\vec{r}, \vec{\Omega}, E). \quad (2.20)$$

The integral on the right-hand side of Eq. (2.20) represents hard collisions, while the integral on the left-hand side of Eq. (2.19) describes soft collisions. Despite the identical form, they describe the energy exchange processes on different scales.

The photon-electron scattering intergral $Q^{\gamma e}$ depends only on photon angular flux. In the absence of Bremsstrahlung production, the photon angular flux is calculated first, and for electron angular flux calculations $Q^{\gamma e}$ is assumed to be a known function. For convenience, $Q^{\gamma e}$ is included into the electron source S in Eq. (2.20) and all subsequent CSD-LBTE equations in this thesis. Also, for brevity, we will drop the superscript ee on the differential cross section as we will solely be considering electron-electron interactions in the scattering integral.

The scattering cross section $\sigma_s(\vec{r}, E' \rightarrow E, \vec{\Omega}' \cdot \vec{\Omega})$ only depends on the scattering angle $\vec{\Omega}' \cdot \vec{\Omega}$ (and not separately on the values of $\vec{\Omega}'$ and $\vec{\Omega}$). One can use this symmetry to expand differential scattering cross section over Legendre polynomials,

$$\sigma_s(\vec{r}, E' \rightarrow E, \vec{\Omega}' \cdot \vec{\Omega}) = \sum_{l=0}^{\infty} (2l+1) \sigma_l(\vec{r}, E' \rightarrow E) P_l(\vec{\Omega}' \cdot \vec{\Omega}). \quad (2.21)$$

Legendre polynomials are related to spherical harmonics by

$$P_l(\vec{\Omega}' \cdot \vec{\Omega}) = \frac{1}{2l+1} \sum_{m=-l}^l Y_{lm}^*(\vec{\Omega}') Y_{lm}(\vec{\Omega}). \quad (2.22)$$

Expansion in Eq. (2.22) transforms the differential cross section in Eq. (2.21) to the following form,

$$\sigma_s(\vec{r}, E' \rightarrow E, \vec{\Omega}' \cdot \vec{\Omega}) = \sum_{l=0}^{\infty} \sum_{m=-l}^l \sigma_l(\vec{r}, E' \rightarrow E) Y_{lm}^*(\vec{\Omega}') Y_{lm}(\vec{\Omega}). \quad (2.23)$$

One can eliminate the integration $\int d\Omega'$ in scattering integral in Eq. (2.20) by expanding the angular flux ψ over angular flux moments ϕ_{lm}

$$\psi(\vec{r}, \vec{\Omega}', E') = \sum_{l'=0}^{\infty} \sum_{m'=-l'}^{l'} \phi_{l'm'}(\vec{r}, E') Y_{l'm'}(\vec{\Omega}'), \quad (2.24)$$

where angular flux moments are found according to

$$\phi_{l'm'}(\vec{r}, E') = \int d\Omega' \psi(\vec{r}, \vec{\Omega}', E') Y_{l'm'}^*(\vec{\Omega}'). \quad (2.25)$$

By plugging Eqs. (2.23) and (2.24) under the integral in Eq. (2.20) and using orthogonality condition for spherical harmonics

$$\int d\Omega' Y_{lm}^*(\vec{\Omega}') Y_{l'm'}(\vec{\Omega}') = \delta_{ll'} \delta_{mm'} \quad (2.26)$$

one obtains CSD LBTE in the form

$$\begin{aligned} & \left[\vec{\Omega} \cdot \vec{\nabla}_r + \sigma(\vec{r}, E) \right] \psi(\vec{r}, \vec{\Omega}, E) - \frac{\partial}{\partial E} \left(\beta_r(\vec{r}, E) \psi(\vec{r}, \vec{\Omega}, E) \right) = \\ & \sum_{l=0}^{\infty} \sum_{m=-l}^l \int_0^{\infty} dE' \sigma_l(\vec{r}, E' \rightarrow E) \phi_{lm}(\vec{r}, E') Y_{lm}(\vec{\Omega}) + S(\vec{r}, \vec{\Omega}, E). \end{aligned} \quad (2.27)$$

For practical calculations, the Legendre coefficients σ_l and angular flux moments

ϕ_{lm} are truncated to an expansion order l_{max} (Lewis and Miller, 1993).

One of the first publications that incorporated a magnetic field into the LBTE was by St-Aubin et al. (2015, 2016). In these papers the authors used reasonable assumptions valid for radiation transport in clinical radiotherapy and the relativistic relation between Lorentz force and particle acceleration to derive the magnetic field terms added to the CSD-LBTE,

$$\left[\vec{\Omega} \cdot \vec{\nabla}_r + \sigma(\vec{r}, E) + \frac{q}{|\vec{p}|} \vec{\tau}(\vec{\Omega}, \vec{B}) \cdot \vec{\nabla}_\Omega \right] \psi(\vec{r}, \vec{\Omega}, E) - \frac{\partial}{\partial E} \left(\beta_r(\vec{r}, E) \psi(\vec{r}, \vec{\Omega}, E) \right) = \sum_{l=0}^{\infty} \sum_{m=-l}^l \int_0^{\infty} dE' \sigma_l(\vec{r}, E' \rightarrow E) \phi_{lm}(\vec{r}, E') Y_{lm}(\vec{\Omega}) + S(\vec{r}, \vec{\Omega}, E). \quad (2.28)$$

The electron charge is denoted by q , and \vec{p} is the relativistic electron momentum.

The magnetic field term in Eq. (2.28) has the form of an angular streaming operator with the vectors $\vec{\tau}$ and $\vec{\nabla}_\Omega$ defined as follows (St-Aubin et al., 2016),

$$\vec{\tau}(\vec{\Omega}, \vec{B}) = \frac{(\vec{\Omega} \times (\vec{\Omega} \times \vec{B}))_z}{\sqrt{1 - \mu^2}} \hat{\varphi} - \frac{(\vec{\Omega} \times \vec{B})_z}{\sqrt{1 - \mu^2}} \hat{\theta}, \quad (2.29)$$

$$\vec{\nabla}_\Omega = \frac{1}{\sqrt{1 - \mu^2}} \hat{\varphi} \frac{\partial}{\partial \varphi} + \hat{\theta} \frac{\partial}{\partial \theta}, \quad (2.30)$$

where $\mu = \cos \theta$ and \vec{B} is the magnetic field.

It should be noted that the term containing the energy derivative on the left-hand side of Eq. (2.28), upon discretization using a diamond difference approximation (Morel, 1985), can be absorbed into scattering term on the right-hand side of Eq. (2.28), and will not appear explicitly in further discussions below. A vacuum

boundary condition is applied to Eq. (2.28) in the solution of the CSD-LBTE,

$$\psi = 0, \quad \vec{\Omega} \cdot \vec{n} < 0 \quad (2.31)$$

where the vector \vec{n} is an outward unit normal that is perpendicular to the boundaries of the system.

2.2 Stationary Iterative Schemes

2.2.1 Overview of Stationary Iterative Solvers

In many practical applications, numerical simulations boil down to finding the solution of systems of linear equations

$$Ax = b. \quad (2.32)$$

The solution is usually found by applying *direct* or *iterative* methods. Direct methods, such as direct factorization methods and the methods based on Gaussian elimination, require $n^3/3$ operations (Isaacson and Keller, 1994), where n is the order of the square matrix A . These methods produce dense intermediate matrices and become impractical for very large n . In addition, rounding errors of basic arithmetic operations on a computer can grow large for large n (Isaacson and Keller, 1994).

Iterative methods are often used to solve large and sparse systems of linear equations. These methods generate a sequence of approximate solutions $\{x^{(t)}\}$, $t =$

$0, 1, 2, \dots$ that, under conditions explained later in the text, converge to a true solution $x = A^{-1}b$. To guarantee solvability, we assume that A is a regular (invertible) matrix.

For such systems solved by iterative methods, matrix inversion operations are abandoned and replaced by matrix-vector multiplication which are less computationally expensive. As a result, iterative methods require fewer operations per iteration. Another advantage of convergent iterative methods is that roundoff errors are “naturally” damped out as the iteration continues (Isaacson and Keller, 1994).

The important characteristics of iterative methods are the convergence rate, the number of computational operations per cycle, the amount of memory required, and the memory access pattern. In what follows we discuss classical iterative methods and address only the first of the characteristics — the rate of convergence. The simplest iterative methods include Richardson’s method, the Jacobi method, and the Gauss-Seidel iteration method.

For a wide class of iterative methods, the iterative form of Eq. (2.32) is often expressed as

$$x^{(t+1)} = \Phi(x^{(t)}, b, A), \quad t = 0, 1, \dots \quad (2.33)$$

where Φ is some function that parametrically depends on b and A . Equation (2.33) is a recurrence relation for two consecutive approximate solutions $x^{(t+1)}$ and $x^{(t)}$. The exact solution represents a fixed point of the iterative Eq. (2.33),

$$x^* = \Phi(x^*, b, A). \quad (2.34)$$

The fixed point x^* in Eq. (2.34), also known as an invariant point, is formally defined as a point in the function's domain that is mapped to itself. Therefore, by definition the fixed point is a true solution of Eq. (2.34).

Linear iterations represent the core of iterative methods for linear systems. They define next iteration as a linear function of a previous iteration. By rearranging matrix $A = M - N$ in Eq. (2.32) with the help of arbitrary nonsingular $n \times n$ matrix M and matrix N , Eq. (2.33) can be written as

$$Mx^{(t+1)} = Nx^{(t)} + b, \quad (2.35)$$

Each choice of M potentially generates an iterative method. The closer the M matrix approximates the inverse of A , the faster the convergence.

Matrices M and N that result from the splitting of matrix A , can be expressed as combinations of the diagonal matrix D , strictly lower and strictly upper triangular matrices L and U respectively of the original matrix $A = D + L + U$. To avoid computationally expansive matrix inversion, the system $M\tilde{x} = \tilde{b}$ should be easy to solve. An additional restriction of non-singularity for M is required ($\det M \neq 0$). Then, Eq. (2.35) generates a unique sequence $\{x^{(t)}\}$ for any initial guess $x^{(0)}$ and constant vector b . The convergent sequence $\{x^{(t)}\}$ will converge to the true solution $x = A^{-1}b$ for all initial vectors $x^{(0)}$.

An important property of every iterative method is the *rate of convergence* which can be described in terms of the eigenvalues of the iteration matrix T ,

$$T = M^{-1}N. \quad (2.36)$$

To see this, let's introduce the definition of the iterative error,

$$e^{(t)} = x^{(t)} - x. \quad (2.37)$$

After subtracting the exact solution x from both sides in Eq. (2.35), one obtains

$$Me^{(t+1)} = Ne^{(t)} \quad (2.38)$$

or,

$$e^{(t+1)} = M^{-1}Ne^{(t)} = Te^{(t)} = T^te^{(0)}. \quad (2.39)$$

The convergence is controlled by the behavior of T^t as $t \rightarrow \infty$ (T^t is a t -th power of matrix T). As can be seen from Eq. (2.39), for convergence to happen the iterative error $e^{(t+1)}$ should asymptotically approach zero, which is equivalent to the condition that $T^t \rightarrow 0$. One can show that the asymptotic behavior of T^t is determined by the largest eigenvalue of T . The initial error in Eq. (2.39) can be expanded over the basis of eigenvectors ξ of matrix T : $e^{(0)} = \sum_{i=1}^n \alpha_i \xi_i(T)$, where $T\xi_i(T) = \lambda_i \xi_i(T)$, and α_i are the expansion coefficients.

Using $e^{(0)}$ in the expansion in Eq. (2.39) results in the following expression for the $(t + 1)$ iterative error

$$e^{(t+1)} = T^te^{(0)} = \sum_{i=1}^n \alpha_i \lambda_i^t \xi_i(T). \quad (2.40)$$

To achieve convergence, all the terms in Eq. (2.40) are required to approach zero in the limit $t \rightarrow \infty$. This condition is satisfied when the eigenvalues $|\lambda_i| < 1$.

Therefore, assuming that M is not singular, convergence of Eq. (2.35) to $x = A^{-1}b$ for all initial guessed solutions $x^{(0)}$ is equivalent to the requirement that the spectral

radius, defined as the modulus of the largest eigenvalue of iteration matrix T , is strictly less than one (Isaacson and Keller, 1994),

$$\rho(T) < 1 \quad (2.41)$$

where,

$$\rho(T) = \max\{|\lambda|: \lambda \in \sigma(T)\}. \quad (2.42)$$

In addition to defining the iterative stability, the spectral radius also serves as an indicative of a convergence rate of the iteration. The spectrum $\sigma(T)$ is a set of all the eigenvalues of matrix T .

Sometimes the spectrum of an iteration matrix T is not easily accessible. In that case, the spectral radius can be quantified based on the properly chosen consistent norm $\|T\|$. For vector-generated (natural) matrix norms, from Eq. (2.39) one obtains

$$\|e^{(t+1)}\| = \|T^t e^{(0)}\| \leq \|T^t\| \cdot \|e^{(0)}\| \leq \|T\|^t \cdot \|e^{(0)}\|. \quad (2.43)$$

The inequality in Eq. (2.43) follows the sufficient condition for convergence,

$$\lim_{t \rightarrow \infty} \|T\|^t = 0, \quad (2.44)$$

which is equivalent to the condition $\|T\| < 1$.

Norm $\|T\|$ is also known as a contraction number of the iteration. Together with the spectral radius, it determines the quality of an iterative method.

In summary, the two conditions that an iterative method should possess are (a) the

inverse of M matrix, resulting from splitting $A = M - N$, should be easily computed, and (b) the spectral radius of the iteration matrix must meet the condition $\rho(M^{-1}N) < 1$.

2.2.2 Source Iteration

In radiation transport, source iteration is the fundamental iterative scheme for solving the LBTE (Larsen E W, 2010; Lewis and Miller, 1993) and is a Gauss-Seidel iterative scheme. SI treats some terms in the transport equation as an iterative source on the right-hand side (RHS) of the equation, and calculates the unknown function on the left-hand side (LHS) of the equation. As a simple example, consider the isotropic LBTE in the absence of a magnetic field

$$\left[\vec{\Omega} \cdot \vec{\nabla}_r + \sigma \right] \psi^{(t)}(\vec{r}, \vec{\Omega}) = \sigma_s \phi^{(t-1)}(\vec{r}) + s(\vec{r}). \quad (2.45)$$

The scalar flux $\phi^{(t-1)}$ on the RHS is considered as a scattering source and is used as an input in t -th iteration cycle to compute the angular flux $\psi^{(t)}(\vec{r}, \vec{\Omega})$. The external source $s(\vec{r})$ is assumed to be a known function. After the solution $\psi^{(t)}$ is found from iteration t , it is used to update to the scalar flux $\phi^{(t)}(\vec{r})$ according to

$$\phi^{(t)}(\vec{r}) = \int d\Omega \psi^{(t)}(\vec{r}, \vec{\Omega}). \quad (2.46)$$

The last equation completes the cycle of the SI procedure. The iterations continue until the solution with a required accuracy is achieved. One of the stopping criteria

used to terminate the iterative process in practical calculations is

$$\frac{\|\phi^{(t+1)} - \phi^{(t)}\|_2}{\|\phi^{(t)}\|_2} \leq 10^{-6}, \quad (2.47)$$

where $\|\cdot\|_2$ is an l^2 vector norm. Equations (2.45) and (2.46) define the unaccelerated source iteration scheme, but accelerated schemes using diffusion synthetic acceleration (DSA) has been applied successfully in the past to the LBTE with no magnetic fields to effectively reduce the spectral radius (Warsa et al., 2004).

2.3 Fourier Analysis Method

When solving problems pertaining to radiation transport and dose deposition, the method of Fourier analysis is a standard tool to investigate the spectral radius of stationary iterative solutions (Golub and Loan, 2012). It is equally applicable to continuous and discrete problems. The usefulness of the Fourier analysis extends to the many problems including those of higher spatial dimensions, and multiple physical variables such as angle, time, and energy. It is capable of not only accurately predicting the spectral radius of an iteration scheme before actual implementation, but also serves as a means for convergence improvement or convergence failure analysis. Regardless of whether the problem is continuous or discrete, Fourier analysis is applied to the equations formulated in terms of the iterative error of the solution f ,

$$\delta f^{(t)}(\vec{r}) = f(\vec{r}) - f^{(t)}(\vec{r}) \quad (2.48)$$

where $f(\vec{r})$ and $f^{(t)}(\vec{r})$ are the exact solution and the solution at iteration (t) respectively. As suggested by Eq. (2.48), this representation is obtained by the subtraction of the iteration equation from the original one.

For continuous problems with an infinite domain a Fourier integral representation for the iterative error takes the form

$$\delta f^{(t)}(\vec{r}) = \int_{-\infty}^{\infty} a^{(t)}(\vec{\lambda}) e^{i\vec{\lambda}\vec{r}} d\vec{\lambda}. \quad (2.49)$$

The iteration equation is then reformulated in terms of coefficients $a^{(t)}(\vec{\lambda})$ of a single Fourier mode

$$a^{(t+1)}(\vec{\lambda}) = \omega(\vec{\lambda}) a^{(t)}(\vec{\lambda}). \quad (2.50)$$

The factor $\omega(\vec{\lambda})$ is called an iteration eigenvalue (Larsen E W, 2010). It is analytically or numerically optimized (maximized) over the Fourier wave number $\vec{\lambda}$. The obtained maximized value characterizes the effectiveness of the iterative procedure. The term ‘eigenvalue’ applied to $\omega(\vec{\lambda})$ is a bit misleading since for continuous equations there is no iteration matrix. Once the iterative equation is discretized, $\omega(\vec{\lambda})$ becomes a matrix, whose largest eigenvalue will define the convergence. Practical applications require the discrete form of the transport equation where the function of interest is defined on a grid — discrete set of points within the domain of the problem definition. The Fourier ansatz in this case assumes that the error function has a form of a Fourier mode,

$$\delta f_{\vec{\lambda}}(\vec{r}) = \delta \tilde{f}_{\vec{\lambda}} e^{i\vec{\lambda}\vec{r}}. \quad (2.51)$$

In this discrete form, an infinite medium can be simulated, by periodically translating an original grid volume element along the coordinate axes X , Y , Z to fill all

the space. For functions with discontinuities on the boundaries, the boundary values inside the translated elements are defined in terms of the boundary values of the original volume element. For example, in a one-dimensional case the left boundary value of translated volume element positioned immediately to the right of the original volume element is defined according to the formula

$$\delta f_\lambda(L^+) = e^{i\lambda L} \delta f_\lambda(0^+), \quad (2.52)$$

where $L^+ = \lim_{\epsilon \rightarrow 0}(L + \epsilon)$, $\epsilon > 0$. Similar definition is applied to 0^+ . The parameter L is the size of original element.

For discrete problems, the iterative convergence of the solution is obtained by finding the modulus of the largest eigenvalue (spectral radius) of the iteration matrix T (Isaacson and Keller, 1994). The iteration matrix is thus defined by the relation

$$f_i^{(t+1)} = T_{ij} f_j^{(t)}, \quad (2.53)$$

where f_i designates the components of the discretized solution on the grid.

Practical simulations tend to generate large systems of linear equations for which an evaluation of the spectral radius by finding the largest eigenvalue can be computationally expensive. For these problems, another approach is used where the spectral radius is estimated as a limiting ratio of successive iterative errors under the assumption of linear convergence to the true solution f according to (Hackbusch, 2016),

$$\rho = \lim_{t \rightarrow \infty} \frac{\|e^{(t)}\|}{\|e^{(t-1)}\|} = \lim_{t \rightarrow \infty} \frac{\|f - f^{(t)}\|}{\|f - f^{(t-1)}\|}. \quad (2.54)$$

For sufficiently large $t \rightarrow \infty$, Eq. (2.48) can be modified to a practical expression of the form,

$$\rho = \lim_{t \rightarrow \infty} \frac{\|f^{(t)} - f^{(t-1)}\|}{\|f^{(t-1)} - f^{(t-2)}\|}. \quad (2.55)$$

In this work, Eq. (2.55) is used to evaluate the spectral radius independently of the Fourier Analysis method and is used to verify the convergence of the systems of equations investigated in this work using previously published code described in (St-Aubin et al., 2015, 2016). This code itself was successfully validated against Monte Carlo methods with 98.9% of points analyzed passing a 2%/2 mm gamma criterion (Low et al., 1998) for clinically realistic radiation transport problems.

2.4 Multigroup Method

An analytical approach to calculating the spectral radius is good for simple confined geometries and infinite homogeneous media. These models provide a good general understanding of the spectral radius of the iterative procedures. However, in practical cases where numerical discretization of the independent variables is used to solve problems with complex spatial geometries, convergence can depend on the numerical procedure. Thus, for the evaluation of the discretized equation spectral radius, we apply a multigroup discretization method in energy (Lewis and Miller, 1993).

The multigroup energy method is a simple discretization method for the energy variable. According to this approach, the domain of the energy variable is divided into a finite number of energy groups (bins) $E_{min} = E_G < \dots < E_g < E_{g-1} < \dots < E_0 = E_{max}$ (Fig. 2.2). The upper limit for the energy variable E_{max} is picked large enough,

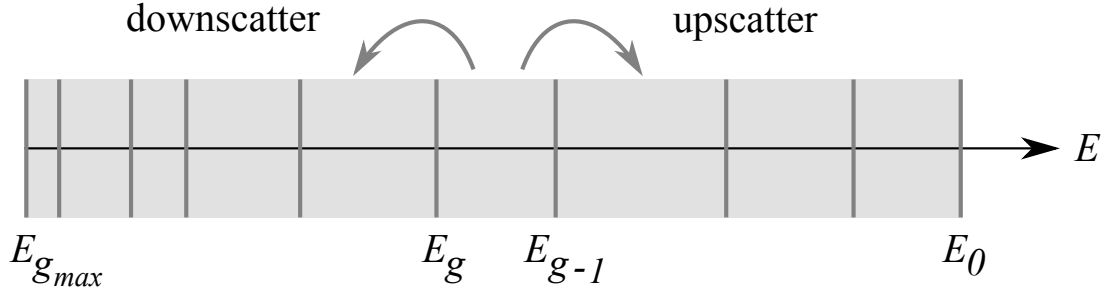


Figure 2.2: Representation of the discretization of the energy variable.

so that the probability of finding a particle with energy exceeding E_{max} is practically zero. The goal of the multigroup method is to reformulate LBTE in terms of group angular fluxes. The solution of the transport equation is obtained for each energy group separately starting from the highest energy group and sequentially moving to the lowest energy group.

The assumption of the multigroup method is that the solution ψ inside every energy group can be represented as a product of two functions $\psi(\vec{r}, \vec{\Omega}, E) \approx f_g(E) \psi_g(\vec{r}, \vec{\Omega})$, where $f_g(E)$ is the weighting function normalized to $\int_{E_g}^{E_{g-1}} dE f_g(E) = 1$, and $\psi_g(\vec{r}, \vec{\Omega}) = \int_{E_g}^{E_{g-1}} dE \psi(\vec{r}, \vec{\Omega}, E)$ is called a group angular flux. The multigroup form of the transport equation is obtained upon integration of LBTE over the energy variable inside an energy group $\int_g dE = \int_{E_g}^{E_{g-1}} dE$. The weighting function f allows the redefinition of the medium and the source parameters of the problem as energy averaged as follows,

$$\sigma_g(\vec{r}) = \int_g dE \sigma(\vec{r}, E) f_g(E), \quad (2.56)$$

$$\sigma_{gg'}(\vec{r}) = \int_g dE \int_{g'} dE' \sigma_s(\vec{r}, E' \rightarrow E) f_g(E'), \quad (2.57)$$

$$S_g(\vec{r}, \vec{\Omega}) = \int_g dE S(\vec{r}, \vec{\Omega}, E). \quad (2.58)$$

The multigroup method is realistic only for slow variations of energy dependent functions within a group. The distribution function $f_g(E)$ can then be approximated by piece-wise constant function. With normalization to unity, it acquires the form $f_g(E) = 1/(\Delta E_g)$ and Eqs. (2.56), (2.57) are re-written as

$$\sigma_g(\vec{r}) = \int_g dE \sigma(\vec{r}, E)/\Delta E_g, \quad (2.59)$$

$$\sigma_{gg'}(\vec{r}) = \int_g dE \int_{g'} dE' \sigma_s(\vec{r}, E' \rightarrow E)/\Delta E_g. \quad (2.60)$$

With these notations, the multigroup energy formulation of the LBTE with magnetic fields acquires the form

$$\left[\vec{\Omega} \cdot \vec{\nabla}_r + \kappa_g \vec{r}(\vec{\Omega}, \vec{B}) \cdot \vec{\nabla}_\Omega + \sigma_g(\vec{r}) \right] \psi_g(\vec{r}, \vec{\Omega}) = \sum_{g'} \sum_{lm} \sigma_{l,gg'}(\vec{r}) \phi_{lm,g'}(\vec{r}) Y_{lm}(\vec{\Omega}) + S_g(\vec{r}, \vec{\Omega}). \quad (2.61)$$

The parameter κ_g in Eq. (2.61) is an energy discretization parameter based on the multigroup method applied to the magnetic field term in Eq. (2.28) (St-Aubin et al., 2016), and is expressed as

$$\kappa_g = \frac{qc}{E_g - E_{g+1}} \ln \left(\frac{E_g + m_0c^2 + \sqrt{(E_g + m_0c^2)^2 - (m_0c^2)^2}}{E_{g+1} + m_0c^2 + \sqrt{(E_{g+1} + m_0c^2)^2 - (m_0c^2)^2}} \right), \quad (2.62)$$

where the electron charge is denoted by q , c is the speed of light in vacuum, and m_0 is the electron mass. When solving the transport Eq. (2.61), the angular flux solution is solved for a single energy group at a time starting from the highest energy group. For brevity, the subscript ‘ g ’ denoting the energy group will be omitted in all subsequent discussions, unless its inclusion is required for clarity.

2.5 Discrete Ordinates Method

In this section, we describe the angular discretization technique known as the Discrete Ordinates method (DOM). Although this method is not used in our calculations, it is still one of the main methods of angular discretization and is used in some commercial applications (Lewis and Miller, 1993) for dose calculations and was used in the work of St-Aubin in the initial calculations of the LBTE with magnetic fields (St-Aubin et al., 2015). At the end we will discuss why we decided to use another approach for angular discretization.

The simple idea of this technique is to solve the integro-differential form of the LBTE at specific angular directions. This method is straightforward to apply when the transport equation does not involve derivatives over the angular variables such as the standard LBTE with no magnetic or electric fields. Below we apply the DOM to the LBTE without magnetic fields, however we refer to the reader to the work of St-Aubin et al. (2015) for the use of the DOM with magnetic fields. With no magnetic fields, the LBTE using the DOM becomes

$$\left[\vec{\Omega}_n \cdot \vec{\nabla}_r + \sigma(\vec{r}) \right] \psi(\vec{r}, \vec{\Omega}_n) = \sum_{lm} \sigma_l(\vec{r}) \phi_{lm}(\vec{r}) Y_{lm}(\vec{\Omega}_n) + S(\vec{r}, \vec{\Omega}_n). \quad (2.63)$$

The index n enumerates the angles for which the equation is solved.

The specific angles chosen are dictated by known quadrature integration rules to allow for the calculation of the angular flux moments,

$$\phi_{lm}(\vec{r}) = \int d\Omega \psi(\vec{r}, \vec{\Omega}) Y_{lm}^*(\vec{\Omega}). \quad (2.64)$$

Equation (2.64) involves an integration over polar and azimuthal angles, θ and φ respectively

$$\int d\Omega = \int_0^\pi \frac{d(\cos \theta)}{2} \int_0^{2\pi} \frac{d\varphi}{2\pi}. \quad (2.65)$$

Integration over Ω can be performed using various quadrature sets, but the work of St-Aubin specifically used square symmetric quadrature sets S_n contain total of $2n^2$ angular directions, with n polar values and $2n$ azimuthal values. Examples of other quadrature sets are triangular and rectangular quadrature sets that derive their names after the shapes that ordinates form on the unit sphere.

To apply this numerical quadrature, the continuous integrals in Eq. (2.65) are transformed to a suitable canonical form

$$\int d\Omega = \frac{1}{2\pi} \int_{-1}^1 d\mu \int_{-1}^1 \frac{d\xi}{\sqrt{1-\xi^2}}. \quad (2.66)$$

The integration over the polar angle in Eq. (2.66) is done using a Gauss-Legendre quadrature rule (Abramowitz and Stegun, 1965; Hildebrand, 1974)

$$\int_{-1}^1 f(\mu) d\mu \approx \sum_{i=1}^n \omega_i f(\mu_i). \quad (2.67)$$

The function $f(\mu)$ is evaluated at the roots of Legendre polynomial $P_n(\mu)$. For an example S_4 quadrature set, the roots of $P_4(\mu)$ are $\mu_1 = -\mu_4 = 0.86113\ 63115\ 94053$, and $\mu_2 = -\mu_3 = 0.33998\ 10435\ 84856$. The weights ω_i are evaluated according to the following formula

$$\omega_i = \frac{2}{(1-\mu_i^2)[P'_n(\mu_i)]^2}, \quad (2.68)$$

and for S_4 are equal to $\omega_1 = \omega_4 = 0.34785\ 48451\ 37454$, and $\omega_2 = \omega_3 = 0.65214\ 51548\ 62546$.

The integration over the azimuthal angle is performed by applying Chebyshev-Gauss method (Abramowitz and Stegun, 1965; Hildebrand, 1974),

$$\int_{-1}^1 \frac{f(\xi) d\xi}{\sqrt{1-\xi^2}} \approx \sum_{i=1}^n \omega_i f(\xi_i). \quad (2.69)$$

The function $f(\xi)$ is evaluated at the roots ξ_i of the Chebyshev polynomial of the first kind $T_n(\xi)$, where

$$\xi_i = \cos\left(\frac{2i-1}{2n}\pi\right), \quad i = 1, n. \quad (2.70)$$

The weight, associated with point ξ_i is $\omega_i = \pi/n$. There are two angles corresponding to the root ξ_i : $\varphi_i = \pi(2i-1)/(2n)$ and $2\pi - \pi(2i-1)/(2n)$. This effectively doubles the number of azimuthal angles on the sphere, making the total number of angular directions at which angular flux ψ_n is evaluated $2n^2$. Because ω_i is a constant weight independent of index i , the final formula for S_4 quadrature integration in angle is

$$\int d\Omega \psi(\theta, \varphi) = \sum_{i=1}^4 \sum_{j=1}^8 \frac{\omega_i^\mu}{16} \psi(\mu_i, \xi_i), \quad (2.71)$$

where ω_i^μ are Gauss-Legendre quadrature weights.

The benefits of discrete ordinate method are its simplicity and low computational complexity. On the other hand, this method can produce inaccurate solutions due to ray effects and false scattering (Chai et al., 1993). False scattering can be attributed to the insufficient spatial discretization of the domain where the angular flux is discontinuous and results in a smearing the intensity distribution. The ray effects are caused by the finite discretization of the angular variables. The DOM has a limited resolution of θ and φ coordinates. It can be eliminated only for the case with a very

high number of directions used.

2.6 Finite Element Method

The Finite Element Method (FEM) has become a standard method for discretizing the spatial variables of the LBTE (Wareing et al, 2001). The FEM applied to the angular variables has gained increasing traction in recent years as a method to overcome the ray effects of the DOM. The FEM originated as a cumulative effort of many scientists over the period of 70 years. Originally, it was proposed by Courant in the 1940s to solve problems of equilibrium and vibration (Jin, 2014). FEM, as we know it today, was formulated by M.J. Turner in 1950–1962¹. Significant contributions to this method were done by other pioneers, such as B.M. Irons, R.J. Melosh, and E.L. Wilson, all coming from the aerospace industry where they spent some parts of their scientific careers¹. Popularization and encouragement to use FEM for solving a wider class of engineering problems is attributed to J.H. Argyris, R.W. Clough, H.C. Martin, and O.C. Zienkiewicz¹. The FEM has been applied to the problems of elasticity, structural analysis, electromagnetics, and a variety of transport problems arising in fluid mechanics, heat transfer, radiations transfer, etc.

Finite element analysis is a powerful method of solving partial differential equations with boundary conditions that describe the behavior of various physical systems. It is based on the general approaches of solving boundary value problems by substituting global basis functions with basis functions of local support.

¹Introduction to Finite Element Methods: <https://www.colorado.edu/engineering/CAS/courses.d/IFEM.d/>

The general outline of the method is discussed as follows. First, consider a boundary value problem defined by a differential equation in operator form (Zohdi, 2014),

$$Lu = q \quad \text{in domain } D, \quad (2.72)$$

subject to problem specific boundary conditions

$$Bu = 0 \quad \text{on domain boundary } \partial D. \quad (2.73)$$

In particle transport two kinds of boundary conditions are used. The explicit boundary conditions that specify explicitly the particle flux distribution on the boundary and implicit boundary conditions which relate incoming and outgoing fluxes and are used to reflect various symmetries of a physical problem.

The operator L is usually a differential or integro-differential operator acting on a sought-for-function u , and q is a known source or driving function. If finding the exact solution of Eq. (2.72) is problematic or impossible, one can attempt to get an approximate solution as a linear combination of predefined approximation functions $\lambda_i(x)$,

$$u_N = \sum_{i=1}^N a_i \lambda_i(x). \quad (2.74)$$

Various conditions are imposed to determine the unknown coefficients a_i in Eq. (2.74) and, as such, these conditions define the method of finding the approximate solution. Substitution of the approximate solution u_N into Eq. (2.72) does not in general turn it into an equality. The difference between the effect of L on approximate solution

u_N and the exact solution u is called the residual,

$$r_N(x) = q - L(u_N). \quad (2.75)$$

One way to find the unknown coefficients a_i is to minimize the residual r_N with respect to some norm $\|r_N\|$. An arbitrary function $u(x)$ is defined by its values at every point in the problem domain as such a pointwise match of such a function by the approximate solution would require a large number (in principle infinite number) of approximation functions. With some assumptions about smoothness of the solution $u(x)$, it can be closely approximated by a moderate number of $\lambda_i(x)$ without imposing too much computational burden. One may wish that $u_N(x)$ match the exact solution $u(x)$ “on average” by minimizing the square of the L_2 norm of the residual defined as

$$\|r_N\|^2 = \int_{D(x)} r_N^2(x) dx. \quad (2.76)$$

Minimization of this norm with respect to a_i results in the system of equations,

$$\int_{D(x)} 2r_N \frac{\partial r_N}{\partial a_i} dx = 0, \quad i = 1, N. \quad (2.77)$$

This method is called the method of least squares. In another approach, one can require that the approximate solution be equal to the exact solution at finite number N of discrete points x_i of the solution domain. That is,

$$r_N(x_i) = 0, \quad i = 1, N. \quad (2.78)$$

Under these conditions, the method is referred as collocation method and can be

rewritten as

$$\int_{D(x)} r_N(x) \delta(x - x_i) dx = 0. \quad (2.79)$$

The discrete ordinate method is a form of collation method. Formal definition of these and similar methods is based on the condition that the integral of the residual $r_N(x)$, weighted by a specific function $\omega(x)$ over the solution domain $D(x)$, is zero. The function $\omega(x)$ is called a weight, and the general name for these methods is the method of weighted residuals.

One important representative of the family of weighted residuals is the Galerkin method, where the weight function $\omega(x)$ is picked from the set of basis functions used to approximate the solution. This is one of the most popular methods applied to a wide variety of problems in science and engineering. The rationale behind this method can be understood by the following example. Consider the error $e_N(x) = u(x) - u_N(x)$ between the true and approximate solutions respectively. If one thinks of $u(x)$ and $u_N(x)$ as vectors in potentially infinite dimensional vector space, then the expansion of $u_N(x)$ over a finite number of basis functions confines $u_N(x)$ to lie in a subspace of $\{\lambda_i(x)\}$, $i = 1, N$ (Fig. **2.3**). The set of basis functions $\{\lambda_i(x)\}$ acts as approximation functions for $u_N(x)$ in Eq. (2.74).

If the true solution also belongs to this subspace, then it is possible to find the expansion coefficients a_i , so that $u_N(x) = u(x)$. If $u(x)$ does not belong to subspace $\{\lambda_i(x)\}$, then one attempts to minimize the error $e_N(x)$ by requiring that, as a vector, $e_N(x)$ be orthogonal to the subspace $\{\lambda_i(x)\}$. In other words, $\langle e_N, \lambda_i \rangle = 0$. Because the $e_N(x)$ is not known in advance, the best option would be to try to orthogonalize $r_N(x) = L(e_N)$ with respect to $\{\lambda_i(x)\}$. This gives N equations to find the expansion

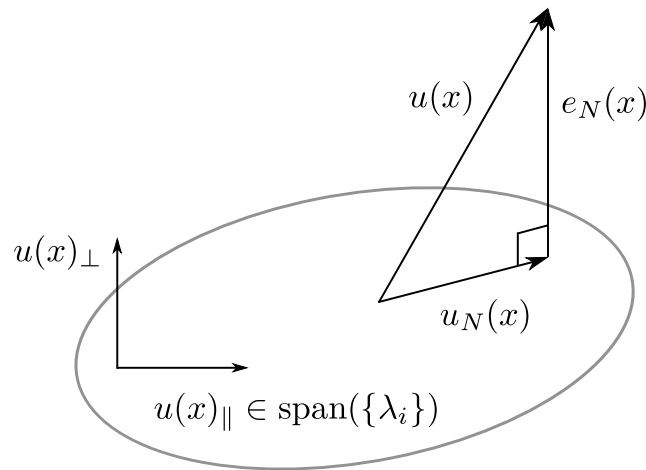


Figure 2.3: Orthogonality of approximate solution and solution error.

coefficients a_i

$$\int_{D(x)} r_N(x) \lambda_i(x) dx = \int_{D(x)} (q - L(u_N)) \lambda_i(x) dx = 0. \quad (2.80)$$

One flaw of the Galerkin approach is that it does not specify a clear way of choosing basis functions, which is related to the problem of possible irregularity of the solution. Finite element analysis, based on the Galerkin approach, solves this by reformulating the differential equation so that the space of the admissible solutions, apart from regular functions, includes functions with less strict differentiability requirements. This is done because many problems of interest possess non-smooth or discontinuous solutions and direct application of Galerkin method as it is described above is not valid. For these problems differentiability of the solution is too restrictive. One of the ways around this is to weaken the regularity requirement. The weak formulation of a boundary value problem is constructed in such a way that it automatically includes regular solutions if they exist.

To derive the weak formulation of a boundary value problem one multiplies Eq. (2.72) by smooth test function $\nu(x)$ and integrates over the solution domain $D(x)$,

$$\int_{D(x)} (q - L(u)) \nu(x) dx = \int_{D(x)} r(x) \nu(x) dx = 0. \quad (2.81)$$

Note that Eqs. (2.80) and (2.81) despite similar look, have different meanings. Equation (2.80) is the orthogonality condition that minimizes the residual r_N with respect to basis functions $\{\lambda_i(x)\}$, while Eq. (2.81) is a formulation of the weak form of a boundary value problem where function $\nu(x)$ is arbitrary.

Below is an example of a weak form of simple boundary value problem. Let's assume that operator $L(u) = (d^2/dx^2)u$. Then using the divergence theorem, one can rewrite Eq. (2.81) as

$$\int_{D(x)} \frac{du}{dx} \frac{d\nu}{dx} dx + \int_{D(x)} q\nu dx - \left. \frac{du}{dx} \nu \right|_{\partial D(x)} = 0. \quad (2.82)$$

It is obvious that in this form the condition of two times differentiability of the solution has been weakened and now requires the existence of only the first derivative.

The next step in the development of FEM is to expand the solution and test function over the basis functions,

$$u(x) \approx \sum_{i=1}^N a_i \lambda_i(x), \quad (2.83)$$

and

$$\nu(x) \approx \sum_{j=1}^N b_j \lambda_j(x). \quad (2.84)$$

Using Eqs. (2.83), (2.84) in Eq. (2.82) will result in the system of linear equations

$$\mathbf{K}A = R, \quad (2.85)$$

where matrix \mathbf{K} and vectors R and A are defined as

$$K_{ji} = \int_{D(x)} \frac{d\lambda_j}{dx} \frac{d\lambda_i}{dx} dx - \lambda_j \frac{d\lambda_i}{dx} \Big|_{\partial D(x)}, \quad (2.86)$$

$$R_j = - \int_{D(x)} q \lambda_j dx, \quad (2.87)$$

$$A_i = a_i. \quad (2.88)$$

It should be noted that function $\nu(x)$ is arbitrary. Therefore, $\forall \nu(x) \rightarrow \forall b_j$. Independence of b_j coefficients is used to obtain matrix Eq. (2.85) from,

$$\sum_{j=1}^N b_j \left(\sum_{i=1}^N K_{ji} a_i - R_j \right) = 0. \quad (2.89)$$

As can be concluded from Eq. (2.89), coefficients b_j do not enter Eq. (2.85).

It was mentioned that Galerkin method does not provide a systematic way of choosing the basis functions λ_i . In our derivations above it is implicitly assumed that the test functions λ_i are defined globally over the whole domain $D(x)$. More often than not, finding global basis functions with the desired behavior on the boundaries and for a given degree of smoothness is not feasible. Finite element analysis eliminates this problem by utilizing basis functions with local support. These functions, though defined globally, vary in a piecewise manner and differ from zero only inside a subdomain of the entire domain, also known as a finite element. Usually, λ_i are chosen to be low degree piecewise polynomials that form a simple nodal basis with

the following conditions

$$\begin{cases} \lambda_i(x_j) = 0, & (i \neq j) \\ \lambda_i(x_i) = 1, \\ \sum_{i=1}^N \lambda_i(x) = 1. \end{cases} \quad (2.90)$$

Basis functions satisfying properties in Eq. (2.90) are also known as Lagrange basis functions.

Here we will provide an example of building a nodal basis in one dimension. This method will be applied later to construct basis in 2D and 3D when solving the LBTE in the space-angle domain. Assume that we are looking for the solution to be a real valued function $u(x)$ of a real valued independent variable $x \in D(x) = [a, b]$. We partition $D(x)$ into N sufficiently small intervals by $N + 1$ node points $\{x_i\}_{i=0}^N$ such that $a = x_0 < x_1 < x_2 \cdots < x_{N-1} < x_N = b$ and assume a linear approximation of the solution $u(x)$ on the interval $I_i[x_{i-1}, x_i]$,

$$\tilde{u}_i(x) = c_0 + c_1x, \quad x \in I_i, \quad c_0, c_1 \in \mathbb{R} \quad (2.91)$$

For simplicity, we write $c_0^i = c_0$, and $c_1^i = c_1$. In Eq. (2.91), $\tilde{u}_i(x)$ is uniquely represented in the monomial basis $\{1, x\}$ by specifying constants c_0, c_1 . There are other ways to uniquely specify the behavior of linear function by providing its values in two different points. In finite element analysis, a linearly approximated function is defined by the values it acquires at the end points of interval $I_i : \alpha_{i-1} = u(x_{i-1})$ and $\alpha_i = u(x_i)$. This method is preferable because the function is specified by its nodal values. Accordingly, the corresponding basis is called a nodal basis $\{\lambda_{i-1}, \lambda_i\}$. In this

basis, the approximate solution is represented as

$$\tilde{u}_i(x) = \alpha_{i-1}\lambda_{i-1}(x) + \alpha_i\lambda_i(x). \quad (2.92)$$

Each basis function $\lambda_i(x)$ is a linear function on I_i with the properties

$$\lambda_j(x_i) = \begin{cases} 1, & i = j \\ 0, & i \neq j \end{cases} \quad (2.93)$$

where $i, j = 0, 1$. The nodal basis on I_i can be defined through the nodal points as follows

$$\lambda_{i-1}(x) = \frac{x_i - x}{x_i - x_{i-1}}, \quad \lambda_i(x) = \frac{x - x_{i-1}}{x_i - x_{i-1}}. \quad (2.94)$$

In the whole domain $D(x)$ the approximation of exact solution $u(x)$ is represented by a piecewise linear function $\tilde{u}(x)$ (see Fig. 2.4).

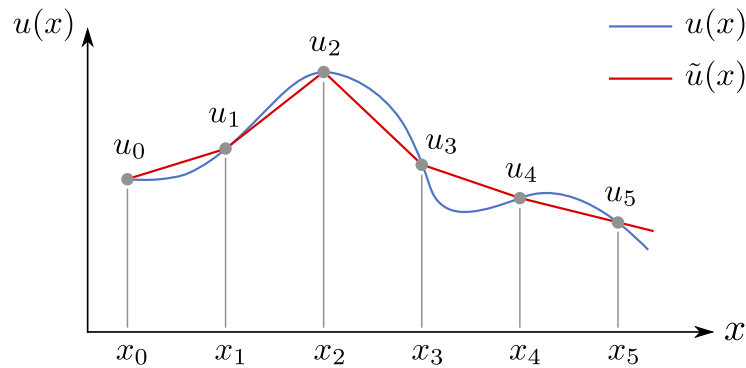


Figure 2.4: Piecewise linear approximation $\tilde{u}(x)$ of the solution $u(x)$.

The nodal values u_i become the degrees of freedom adjusted to find the best approximation of $u(x)$. The function $\lambda_i(x)$ for node x_i has a local support and is defined on $I_i \cup I_{i+1}$, except the leftmost and rightmost basis functions that are defined only on I_1 and I_N respectively. In summary, approximation $\tilde{u}(x)$ is sought in the form

of linear expansion

$$u(x) \approx \tilde{u}(x) = \sum_{i=0}^N u_i \lambda_i(x) \quad (2.95)$$

over the basis functions

$$\lambda_i(x) = \begin{cases} \frac{x - x_{i-1}}{x_i - x_{i-1}}, & x \in I_i \\ \frac{x_{i+1} - x}{x_{i+1} - x_i}, & x \in I_{i+1} \\ 0, & \text{otherwise} \end{cases} \quad (2.96)$$

The hat-shaped basis functions $\lambda_i(x)$ are depicted in Fig. (2.5).

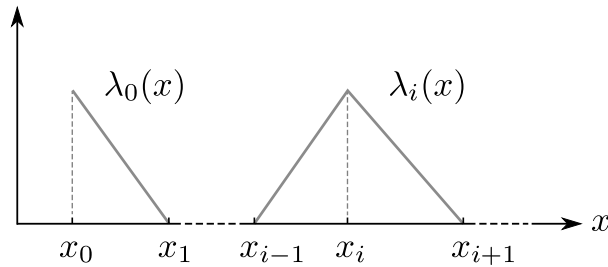


Figure 2.5: Hat-shaped basis functions used in linear piecewise approximation.

In the application of finite element analysis to solve Linear Boltzmann transport equation with magnetic field our numerical simulations follow the procedure:

1. Generate mesh in solution domain. This is required to discretize the continuous solution domain into finite elements where the discrete solution is found at the nodes of the elements.
2. Select and construct basis functions.
3. Reformulate LBTE in a weak form.

4. Represent LBTE in a matrix form.

The solution of the matrix equation will be addressed in chapters 4 and 5. We restate LBTE here again for convenience. The angular flux in a magnetic field is found by solving the following equation,

$$\left[\vec{\Omega} \cdot \vec{\nabla}_r + \kappa \vec{r}(\vec{\Omega}, \vec{B}) \cdot \vec{\nabla}_\Omega + \sigma(\vec{r}) \right] \psi(\vec{r}, \vec{\Omega}) = \sum_{lm} \sigma_l(\vec{r}) \phi_{lm}(\vec{r}) Y_{lm}(\vec{\Omega}) + S(\vec{r}, \vec{\Omega}) \quad (2.97)$$

The connection between angular flux ψ and angular flux moments ϕ_{lm} is given by

$$\phi_{lm}(\vec{r}) = \int d\Omega \psi(\vec{r}, \vec{\Omega}) Y_{lm}^*(\vec{\Omega}). \quad (2.98)$$

Here we would like to state the definition of the integration norm over the solid angle $d\Omega$ and the normalization for spherical harmonics. We use the convention where the integration over unit sphere produces unity,

$$\int d\Omega \int_0^{2\pi} \frac{d\varphi}{2\pi} \int_{-1}^1 \frac{d\mu}{2} = 1, \quad (2.99)$$

where $\mu = \cos \theta$. With this convention spherical harmonics do not contain $1/\sqrt{4\pi}$ in their normalization factor.

For a particular energy group, the angular flux depends on five independent variables: two angular variables θ and φ , and three spatial components of radius vector x , y , and z . The solution is defined on $\mathbb{R}^3 \times \mathbb{S}^2$, where \mathbb{S}^2 is a two-dimensional unit sphere, and \mathbb{R}^3 is a three-dimensional real space. The solution is first found within a finite cube $L^3 = \{(x, y, z) \in \mathbb{R}^3 \mid 0 \leq x, y, z \leq L\}$. To model an infinite domain, the finite cube is then periodically extended over all space \mathbb{R}^3 .

2.6.1 Angular Domain Discretization

Following the first step of our procedure of the previous section, we partition the solution domain into finite elements. The meshing of the angular domain \mathbb{S}^2 is done in two steps. First, the unit sphere is tessellated into spherical triangles (Fig. 2.6), which tessellation is then unwrapped onto a flat 2D grid (St-Aubin et al 2016). In constructing a grid, one should pay attention that all the finite elements are connected to each other only by their vertices. Also, the grid should not contain any gaps. In practical calculations the angular grid is chosen to be the same for the entire spatial domain regardless of possible variations in the medium density.

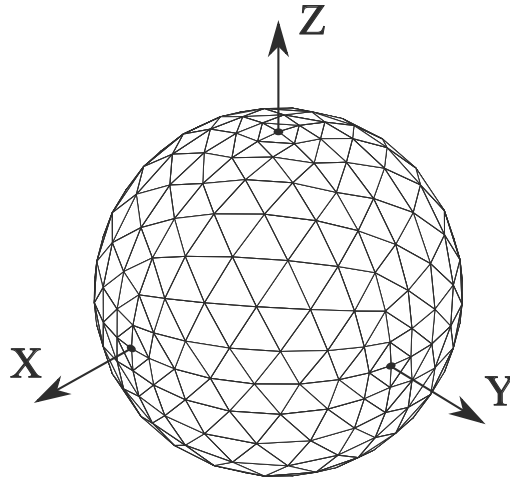


Figure 2.6: An example tessellation of the angular domain on the unit sphere. This tessellation contains 512 elements.

The angular mesh used in this work is composed of 40 triangles on the flattened grid (Fig. 2.7). This number of finite elements was verified to be sufficient to correctly calculate the spectral radius for homogeneous medium while minimizing matrix size and calculation time.

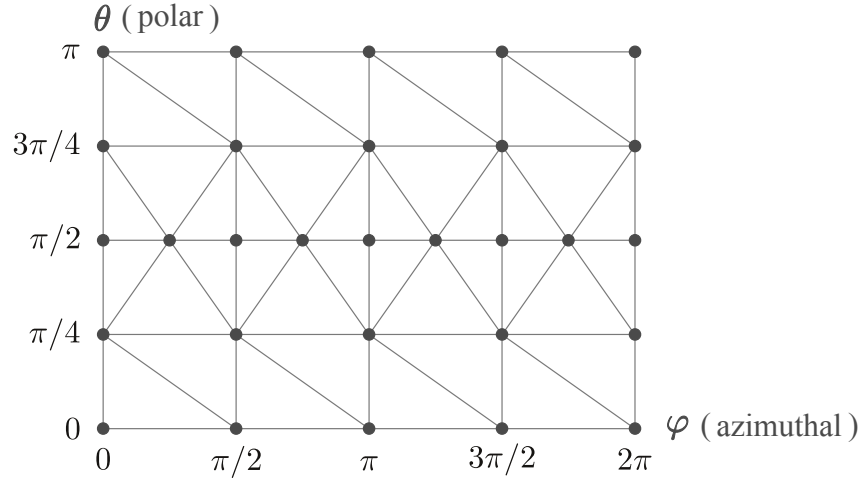


Figure 2.7: A 40 element tessellation is unwrapped onto a flat 2D surface with some points added at the poles $\theta = 0, \pi$.

To reduce numerical errors, a Delaunay triangulation is performed such that the triangles of the mesh to maximize the inner angles (Jin, 2014). For this reason, several points were added to the poles at $\theta = 0$, and π . Despite the fact that there is no one-to-one mapping between the surface of the unit sphere \mathbb{S}^2 and rectangle $\{(\varphi, \theta), 0 \leq \varphi \leq 2\pi, 0 \leq \theta \leq \pi\}$ in \mathbb{R}^2 , addition of these points to the mesh does not affect the results of simulation.

In our simulations, we use a linear angular basis based on what was performed previously (St-Aubin et al., 2016). That is, on every finite element the unknown function is approximated by a plane,

$$f^p(\varphi, \theta) = a^p + b^p\varphi + c^p\theta \quad (2.100)$$

where a^p , b^p , and c^p are unknown coefficients. Higher order polynomial basis functions can also be used as a means to reduce the number of finite elements and/or to increase the accuracy of calculations.

Transition from a degree 1 polynomial basis to nodal basis employs the following relations as an intermediate step,

$$f_i^p = a^p + b^p \varphi_i + c^p \theta_i, \quad i = 1, 2, 3. \quad (2.101)$$

The matrix form of the system of equations shown in Eq. (2.101) is

$$\begin{pmatrix} 1 & \varphi_1 & \theta_1 \\ 1 & \varphi_2 & \theta_2 \\ 1 & \varphi_3 & \theta_3 \end{pmatrix} \begin{pmatrix} a^p \\ b^p \\ c^p \end{pmatrix} = \begin{pmatrix} f_1^p \\ f_2^p \\ f_3^p \end{pmatrix} \quad (2.102)$$

Here, (φ_i, θ_i) are the coordinates of i -th node in the p -th element. Inverting the system of Eqs. (2.101) with respect to a^p , b^p , and c^p allows the expression of $f^p(\varphi, \theta)$ in a nodal basis,

$$f^p(\varphi, \theta) = \sum_{i=1}^3 f_i^p \gamma_i^p(\varphi, \theta). \quad (2.103)$$

In Eqs. (2.101–2.103), f_i^p is a function's value at node i , and $\gamma_i^p(\varphi, \theta)$ is the basis function, associated with the same node,

$$\gamma_i^p(\varphi, \theta) = \frac{1}{2A^p} (a_i^p + b_i^p \varphi + c_i^p \theta), \quad i = 1, 2, 3 \quad (2.104)$$

where A^p designates the area of the p -th element expressed by the formula

$$A^p = \frac{1}{2} \det \begin{pmatrix} 1 & \varphi_1 & \theta_1 \\ 1 & \varphi_2 & \theta_2 \\ 1 & \varphi_3 & \theta_3 \end{pmatrix}. \quad (2.105)$$

The coefficients (a_i^p, b_i^p, c_i^p) of the basis functions in Eq. (2.104) depend on coordi-

nates of the nodes in the following way,

$$\begin{aligned}
 a_1^p &= \varphi_2^p \theta_3^p - \varphi_3^p \theta_2^p, & b_1^p &= \theta_2^p - \theta_3^p, & c_1^p &= \varphi_3^p - \varphi_2^p, \\
 a_2^p &= \varphi_3^p \theta_1^p - \varphi_1^p \theta_3^p, & b_2^p &= \theta_3^p - \theta_1^p, & c_2^p &= \varphi_1^p - \varphi_3^p, \\
 a_3^p &= \varphi_1^p \theta_2^p - \varphi_2^p \theta_1^p, & b_3^p &= \theta_1^p - \theta_2^p, & c_3^p &= \varphi_2^p - \varphi_1^p.
 \end{aligned} \tag{2.106}$$

The basis functions in Eq. (2.104) for element p are depicted in Fig. (2.8).

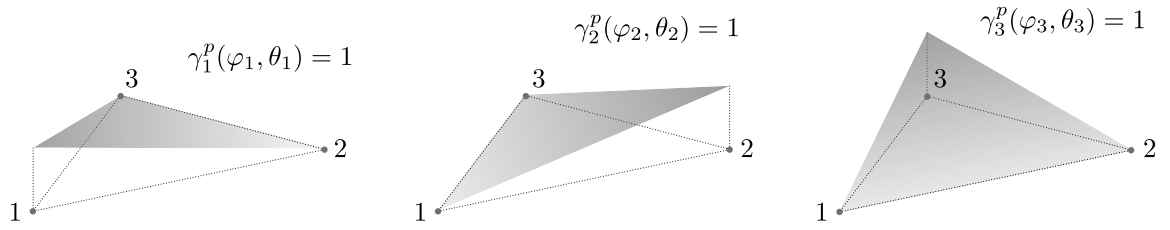


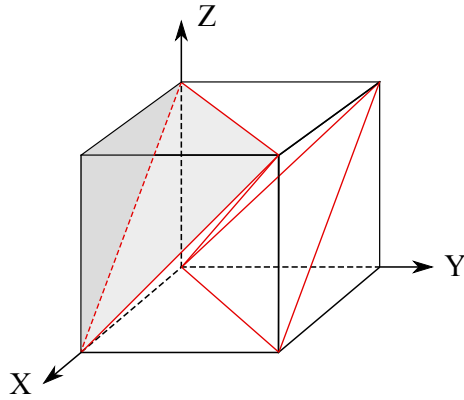
Figure 2.8: Basis functions $\gamma_i^p(\varphi, \theta)$ represent pieces of 2D plane in 3D and acquire unity at node i and zero at opposite side of triangle.

2.6.2 Spatial Domain Discretization

In the spatial domain, the cube L^3 is divided into six tetrahedral elements of equal volume. It is the minimal number of spatial elements consistent with the condition of periodic translation. Figure (2.9) shows the main L^3 cube at the origin with one of the elements highlighted in grey.

In complete analogy with the angular domain, in the spatial domain we utilize a linear approximation for the unknown function inside a tetrahedral element k ,

$$F^k(x, y, z) = a^k + b^k x + c^k y + d^k z. \tag{2.107}$$

Figure 2.9: Partition of L^3 cube into spatial 3D finite elements.

To find the nodal representation, one derives unknown coefficients a^k, b^k, c^k , and d^k by inverting matrix Eq. (2.108),

$$\begin{pmatrix} 1 & x_1 & y_1 & z_1 \\ 1 & x_2 & y_2 & z_2 \\ 1 & x_3 & y_3 & z_3 \\ 1 & x_4 & y_4 & z_4 \end{pmatrix} \begin{pmatrix} a^k \\ b^k \\ c^k \\ d^k \end{pmatrix} = \begin{pmatrix} F_1^k \\ F_2^k \\ F_3^k \\ F_4^k \end{pmatrix}. \quad (2.108)$$

For a^k, b^k, c^k , and d^k one obtains,

$$a^k = \frac{1}{6V^k} \det \begin{pmatrix} F_1^k & F_2^k & F_3^k & F_4^k \\ x_1^k & x_2^k & x_3^k & x_4^k \\ y_1^k & y_2^k & y_3^k & y_4^k \\ z_1^k & z_2^k & z_3^k & z_4^k \end{pmatrix} = \frac{1}{6V^k} (a_1^k F_1^k + a_2^k F_2^k + a_3^k F_3^k + a_4^k F_4^k), \quad (2.109)$$

$$b^k = \frac{1}{6V^k} \det \begin{pmatrix} 1 & 1 & 1 & 1 \\ F_1^k & F_2^k & F_3^k & F_4^k \\ y_1^k & y_2^k & y_3^k & y_4^k \\ z_1^k & z_2^k & z_3^k & z_4^k \end{pmatrix} = \frac{1}{6V^k} (b_1^k F_1^k + b_2^k F_2^k + b_3^k F_3^k + b_4^k F_4^k), \quad (2.110)$$

$$c^k = \frac{1}{6V^k} \det \begin{pmatrix} 1 & 1 & 1 & 1 \\ x_1^k & x_2^k & x_3^k & x_4^k \\ F_1^k & F_2^k & F_3^k & F_4^k \\ z_1^k & z_2^k & z_3^k & z_4^k \end{pmatrix} = \frac{1}{6V^k} (c_1^k F_1^k + c_2^k F_2^k + c_3^k F_3^k + c_4^k F_4^k), \quad (2.111)$$

$$d^k = \frac{1}{6V^k} \det \begin{pmatrix} 1 & 1 & 1 & 1 \\ x_1^k & x_2^k & x_3^k & x_4^k \\ y_1^k & y_2^k & y_3^k & y_4^k \\ F_1^k & F_2^k & F_3^k & F_4^k \end{pmatrix} = \frac{1}{6V^k} (d_1^k F_1^k + d_2^k F_2^k + d_3^k F_3^k + d_4^k F_4^k), \quad (2.112)$$

where V^k denotes the volume of the finite element k ,

$$V^k = \frac{1}{6} \det \begin{pmatrix} 1 & 1 & 1 & 1 \\ x_1^k & x_2^k & x_3^k & x_4^k \\ y_1^k & y_2^k & y_3^k & y_4^k \\ z_1^k & z_2^k & z_3^k & z_4^k \end{pmatrix}. \quad (2.113)$$

In this nodal basis, the F^k function is expressed by

$$F^k(x, y, z) = \sum_{i=1}^4 F_i^k L_i^k(x, y, z), \quad (2.114)$$

where the nodal basis functions $L_i^k(x, y, z)$ are defined as

$$L_i^k(x, y, z) = \frac{1}{6V^k} \left(a_i^k + b_i^k x + c_i^k y + d_i^k z \right). \quad (2.115)$$

2.6.3 Discontinuous Galerkin Finite Element Method

Even though conventional Galerkin method can be applied to broader class of equations that includes self-adjoint and non-self-adjoint equations, its use in the latter case must done with care. Differential operators of odd order equations are not self-adjoint (such as the LBTE). In practice, application of the Galerkin method to this class of equations is unsuitable and leads to numerical oscillations in the solution, and can even lead to instability (Jiang, 1998). The use of a discontinuous Galerkin method has been shown to stabilize the LBTE and accurately model discontinuities in the angular flux due to discontinuities in the material and density in the patient. Discontinuities are accounted by removing spatial and angular derivatives using Gauss theorem and applying proper boundary conditions at the border of each finite element. Stabilization is achieved when the solution is found by sweeping through the mesh in the direction of transport propagation – a process also known as upwind stabilization (Lewis and Miller, 1993).

In this section we apply the discontinuous Galerkin FEM (DFEM) to the LBTE

with magnetic fields. To obtain the weak form of the LBTE with magnetic fields in the DFEM formulation, we need to form the scalar product of Eq. (2.97) with the combined basis $\gamma_\alpha^p(\varphi, \theta) \otimes L_i^k(x, y, z)$ which for simplicity we will write as $\gamma_\alpha^p L_i^k$ assuming proper arguments. The integration of the scalar product is over the volume V^k and the area of the angular element A^p . We also assume a homogeneous medium, so that the material total and differential cross sections are constants over the spatial domain. Thus the FEM applied to Eq. (2.97),

$$\begin{aligned}
& \int_{V^k} \int_{A^p} \vec{\Omega} \cdot \left(\vec{\nabla}_r \psi(\vec{r}, \vec{\Omega}) \right) \gamma_\alpha^p L_i^k dV dA \\
& + \int_{V^k} \int_{A^p} \kappa \vec{\tau}(\vec{\Omega}, \vec{B}) \cdot \left(\vec{\nabla}_\Omega \psi(\vec{r}, \vec{\Omega}) \right) \gamma_\alpha^p L_i^k dV dA \\
& + \sigma \int_{V^k} \int_{A^p} \psi(\vec{r}, \vec{\Omega}) \gamma_\alpha^p L_i^k dV dA \\
& = \int_{V^k} \int_{A^p} \sum_{lm} \sigma_l Y_{lm}(\vec{\Omega}) \int d\Omega' \psi(\vec{r}, \vec{\Omega}') Y_{lm}^*(\vec{\Omega}') \gamma_\alpha^p L_i^k dV dA \\
& + \int_{V^k} \int_{A^p} S(\vec{r}, \vec{\Omega}) \gamma_\alpha^p L_i^k dV dA.
\end{aligned} \tag{2.116}$$

We now expand the unknown function over the same basis $\gamma_\alpha^p L_i^k$,

$$\psi(\vec{r}, \vec{\Omega}) = \sum_{i'=1}^4 \sum_{\alpha'=1}^3 \psi_{\alpha', i'}^{p, k} \gamma_{\alpha'}^p L_{i'}^k. \tag{2.117}$$

To apply the DFEM to Eq. (2.116) we apply Gauss's theorem to the first term in Eq. (2.116) (spatial streaming term), and integration by parts to the second term in Eq. (2.116) (magnetic field angular streaming term). In this way possible solution discontinuities can be properly incorporate on the boundaries through the integration over the surface of the spatial finite elements and edges of the angular elements. The detailed description of Gauss's theorem to the (first) spatial streaming term in

Eq. (2.116) and its matrix formulation is presented below,

$$\begin{aligned}
& \int_{V^k} \int_{AP} \vec{\Omega} \cdot \left(\vec{\nabla}_r \psi(\vec{r}, \vec{\Omega}) \right) \gamma_\alpha^p L_i^k dV dA = \\
& - \int_{V^k} \int_{AP} \psi(\vec{r}, \vec{\Omega}) \gamma_\alpha^p \vec{\Omega} \cdot \left(\vec{\nabla}_r L_i^k \right) dV dA + \int_{\partial V^k} \int_{AP} \psi(\vec{r}, \vec{\Omega}) \gamma_\alpha^p L_i^k \vec{\Omega} \cdot d\vec{S} dA \\
& = - \sum_{i'=1}^4 \sum_{\alpha'=1}^3 \vec{C}_{ii'}^k \vec{A}_{\alpha\alpha'}^p \psi_{\alpha',i'}^{p,k} + \sum_{i'=1}^4 \sum_{\alpha'=1}^3 \vec{B}_{ii'}^k \vec{A}_{\alpha\alpha'}^p \psi_{\alpha',i'}^{p,k} \quad (2.118)
\end{aligned}$$

where matrices $\vec{A}_{\alpha\alpha'}^p$, $\vec{B}_{ii'}^k$, and $\vec{C}_{ii'}^k$ are defined as follows

$$\vec{A}_{\alpha\alpha'}^p = \int_{AP} \gamma_\alpha^p \gamma_{\alpha'}^p \vec{\Omega} dA, \quad (2.119)$$

$$\vec{B}_{ii'}^k = \int_{\partial V^k} L_{i'}^k L_i^k d\vec{S}, \quad (2.120)$$

$$\vec{C}_{ii'}^k = \int_{V^k} L_{i'}^k \left(\vec{\nabla}_r L_i^k \right) dV. \quad (2.121)$$

In a similar way to Eq. (2.118), the magnetic field angular streaming (second term in Eq. (2.116) can be rederived using integration by parts, and all terms can be placed in a matrix form, so that final discretized LBTE (in matrix operator form) is

$$\begin{aligned}
& \sum_{i'=1}^4 \sum_{\alpha'=1}^3 \left[\vec{B}_{ii'}^k \vec{A}_{\alpha\alpha'}^p - \vec{C}_{ii'}^k \vec{A}_{\alpha\alpha'}^p + \kappa D_{ii'}^k F_{\alpha\alpha'}^p - \kappa D_{ii'}^k H_{\alpha\alpha'}^p + \sigma D_{ii'}^k G_{\alpha\alpha'}^p \right] \psi_{\alpha',i'}^{p,k} = \\
& \sum_{i'=1}^4 \sum_{\alpha'=1}^3 \sum_{lm} \sigma_l \sum_{\tilde{p}=1}^{N_{\tilde{p}}} D_{ii'}^k J_\alpha^p \left(J_\alpha^{\tilde{p}} \right)^* \psi_{\alpha',i'}^{\tilde{p},k} + S_{\alpha,i}^{p,k}, \quad (2.122)
\end{aligned}$$

where the definition of other matrices is

$$D_{ii'}^k = \int_{V^k} L_{i'}^k L_i^k dV, \quad (2.123)$$

$$G_{\alpha\alpha'}^p = \int_{A^p} \gamma_\alpha^p \gamma_{\alpha'}^p dA, \quad (2.124)$$

$$F_{\alpha\alpha'}^p = \int_{\partial A^p} \gamma_\alpha^p \gamma_{\alpha'}^p \vec{\tau}(\vec{\Omega}, \vec{B}) d\vec{\Gamma}, \quad (2.125)$$

$$H_{\alpha\alpha'}^p = \int_{A^p} \vec{\nabla}_\Omega \left(\vec{\tau}(\vec{\Omega}, \vec{B}) \gamma_\alpha^p \right) \gamma_{\alpha'}^p dA, \quad (2.126)$$

$$J_\alpha^p = \int_{A^p} \gamma_{\alpha'}^p Y_{lm}(\vec{\Omega}) dA, \quad (2.127)$$

$$S_{\alpha,i}^{p,k} = \int_{V^k} \int_{A^p} S(\vec{r}, \vec{\Omega}) L_i^k \gamma_\alpha^p dV dA. \quad (2.128)$$

In Eqs. (2.119–2.121) and (2.123–2.128) integration $\int_{\partial V^k} [\cdot] d\vec{S}$ is over the surface of the volume element V^k , and integration $\int_{\partial A^p} [\cdot] d\vec{\Gamma}$ is over the contour of the 2D finite element A^p on the sphere. The final discontinuous description of the discrete form of LBTE with magnetic fields is accompanied by the boundary conditions in spatial domain,

$$\psi_{ip,k} = \begin{cases} \psi_{\alpha,i}^{inc}, & \vec{\Omega} \cdot \vec{n}_i \leq 0 \\ \psi_{\alpha,i}, & \vec{\Omega} \cdot \vec{n}_i > 0 \end{cases} \quad (2.129)$$

and in the angular domain,

$$\psi_{ip,k'} = \begin{cases} \psi_{\alpha,i}^{inc}, & \vec{\tau}(\vec{\Omega}, \vec{B}) \cdot \vec{n}_\alpha \leq 0 \\ \psi_{\alpha,i}, & \vec{\tau}(\vec{\Omega}, \vec{B}) \cdot \vec{n}_\alpha > 0 \end{cases}. \quad (2.130)$$

The boundary conditions for a spatial element in Eq. (2.129) are expressed in terms of outward normal \vec{n}_i on face i and is related to the $d\vec{S}$ surface element in Eq. (2.120) as $d\vec{S} = \vec{n}_i dS$. Similarly, \vec{n}_α in Eq. (2.130) expresses the outward normal to the edge α

of angular element and is related to $d\vec{\Gamma}$ in Eq. (2.125) by $d\vec{\Gamma} = \vec{n}_\alpha d\Gamma$. The superscript *inc* on the angular flux for the boundary conditions in Eqs. (2.129), (2.130) denotes incoming angular flux flowing through a spatial face, or angular edge.

Equations (2.119–2.130) constitute the boundary value problem for discrete LBTE, the iterative solution of which is discussed in chapters 4 and 5.

Chapter 3

Analysis of the Spectral Radius in an Infinite Medium — Continuous LBTE

3.1 Continuous LBTE with no Magnetic Fields

The spectral radius of the iterative solution of the continuous LBTE in a homogeneous medium in the presence of a magnetic field is investigated first. For an infinite domain, it is possible in some cases to extract an analytical expression for the spectral radius as a function of external parameters such as magnetic field strength, material density, and degree of anisotropy as expressed by the maximum Legendre expansion order l_{max} .

To establish a solid ground for calculations with magnetic fields, we first derive the

spectral radius for the case of an infinite medium with zero magnetic field and compare it with previously published results. The starting point is the time-independent transport equation with no magnetic field for an energy group g ,

$$\left[\vec{\Omega} \cdot \vec{\nabla}_r + \sigma_g \right] \psi_g(\vec{r}, \vec{\Omega}) - \sum_{g'=1}^{N_G} \int d\Omega' \sigma_{s,gg'}(\vec{\Omega} \cdot \vec{\Omega}') \psi_{g'}(\vec{r}, \vec{\Omega}') = S_g(\vec{r}, \vec{\Omega}). \quad (3.1)$$

For an isotropic problem, which we consider first, the scattering probability is the same in all directions. Physically this usually happens for low particle energies. Under these conditions, there is no angular dependence for the group-to-group differential cross section $\sigma_{s,gg'}(\vec{\Omega} \cdot \vec{\Omega}') \rightarrow \sigma_{s,gg'}$ or the external source $S_g(\vec{r}, \vec{\Omega}) \rightarrow S_g(\vec{r})$. The summation index g' is over all N_G energy groups. Integration over Ω' in Eq. (3.1) results in a simplified transport equation in terms of angular flux ψ and scalar flux ϕ dependent variables,

$$\left[\vec{\Omega} \cdot \vec{\nabla}_r + \sigma_g \right] \psi_g(\vec{r}, \vec{\Omega}) = \sigma_{s,gg} \phi_g(\vec{r}) + s_g(\vec{r}), \quad (3.2)$$

$$\phi_g(\vec{r}) = \int d\Omega \psi_g(\vec{r}, \vec{\Omega}), \quad (3.3)$$

where,

$$s_g(\vec{r}) = \sum_{g' \neq g}^{N_G} \sigma_{s,gg'} \phi_{g'}(\vec{r}) + S_g(\vec{r}). \quad (3.4)$$

In what follows we will consider the transport equation for a particular energy group and, therefore as before, drop the energy group index to simplify our notations.

To obtain the solution of Eq. (3.2) through an iterative solution technique, we regard the scattering term (first term on the right-hand side of Eq. (3.2)) as a known iterative source that is used to calculate the unknown values on the left-hand side of

equation. According to the multigroup approach, the solution is first found for the highest energy bin and then proceeds in the direction of lower energy bins. For a particular energy bin g , the solution in higher energy bins ($E_{g'} > E_g$) is known and does not change during within-group iterations. Therefore, the term $s_g(\vec{r})$ in Eq. (3.4) is constant and does not possess an iteration index.

Defining (t) to be an iteration index, this transforms Eqs. (3.2), (3.3) to the iterative form of the source iteration procedure as described in (subsection 2.2.2),

$$\left[\vec{\Omega} \cdot \vec{\nabla}_r + \sigma \right] \psi^{(t+1)}(\vec{r}, \vec{\Omega}) = \sigma_s \phi^{(t)}(\vec{r}) + s(\vec{r}), \quad (3.5)$$

$$\phi^{(t)}(\vec{r}) = \int d\Omega \psi^{(t)}(\vec{r}, \vec{\Omega}). \quad (3.6)$$

Next, we construct the iterative differences for angular and scalar flux variables,

$$\delta\psi^{(t+1)}(\vec{r}, \vec{\Omega}) = \psi^{(t+1)}(\vec{r}, \vec{\Omega}) - \psi^{(t)}(\vec{r}, \vec{\Omega}), \quad (3.7)$$

$$\delta\phi^{(t+1)}(\vec{r}) = \phi^{(t+1)}(\vec{r}) - \phi^{(t)}(\vec{r}). \quad (3.8)$$

Reformulation of Eqs. (3.5), (3.6) in terms of $\delta\psi$ and $\delta\phi$ produces the following system of equations, used to find the spectral radius,

$$\left[\vec{\Omega} \cdot \vec{\nabla}_r + \sigma \right] \delta\psi^{(t+1)}(\vec{r}, \vec{\Omega}) = \sigma_s \delta\phi^{(t)}(\vec{r}), \quad (3.9)$$

$$\delta\phi^{(t)}(\vec{r}) = \int d\Omega \delta\psi^{(t)}(\vec{r}, \vec{\Omega}). \quad (3.10)$$

As was mentioned in section 2.3, in Fourier analysis both $\delta\psi$ and $\delta\phi$ functions are

sought in the form of Fourier modes,

$$\delta\psi^{(t)}(\vec{r}, \vec{\Omega}) = \int_{-\infty}^{\infty} a^{(t)}(\vec{\lambda}, \vec{\Omega}) e^{i\vec{\lambda}\vec{r}} d\vec{\lambda}, \quad (3.11)$$

$$\delta\phi^{(t)}(\vec{r}) = \int_{-\infty}^{\infty} b^{(t)}(\vec{\lambda}) e^{i\vec{\lambda}\vec{r}} d\vec{\lambda}. \quad (3.12)$$

Application of Eqs. (3.11), (3.12) together with the mutual independence of Fourier modes transforms Eqs. (3.9), (3.10) to the following system of integro-algebraic equations

$$\left[i\vec{\Omega} \cdot \vec{\lambda} + \sigma \right] a^{(t+1)}(\vec{\lambda}, \vec{\Omega}) = \sigma_s b^{(t)}(\vec{\lambda}), \quad (3.13)$$

$$b^{(t)}(\vec{\lambda}) = \int d\Omega a^{(t)}(\vec{\lambda}, \vec{\Omega}). \quad (3.14)$$

This system can be converted to an eigenvalue problem by solving for $a^{(t)}$ in Eq. (3.13) and substituting into Eq. (3.14),

$$b^{(t)}(\vec{\lambda}) = \left[\int d\Omega \frac{\sigma_s}{i\vec{\Omega} \cdot \vec{\lambda} + \sigma} \right] b^{(t-1)}(\vec{\lambda}) = \omega(\vec{\lambda}) b^{(t-1)}(\vec{\lambda}). \quad (3.15)$$

The expression for $\omega(\vec{\lambda})$ is defined as,

$$\omega(\vec{\lambda}) = \int d\Omega \frac{\sigma_s}{i\vec{\Omega} \cdot \vec{\lambda} + \sigma}, \quad (3.16)$$

which is interpreted as an eigenvalue of the iterative operator that corresponds to the eigenfunction $\exp(i\vec{\lambda}\vec{r})$. As explained in section 2.3, the spectral radius ρ , by

definition, is the modulus of the largest eigenvalue,

$$\rho \equiv \sup_{\vec{\lambda}} |\omega(\vec{\lambda})|. \quad (3.17)$$

To evaluate the integral in Eq. (3.16), we split it into real and complex parts,

$$\omega(\vec{\lambda}) = \sigma_s \int d\Omega \frac{\sigma}{\sigma^2 + (\vec{\Omega} \cdot \vec{\lambda})^2} - \sigma_s \int d\Omega \frac{i \vec{\Omega} \cdot \vec{\lambda}}{\sigma^2 + (\vec{\Omega} \cdot \vec{\lambda})^2}. \quad (3.18)$$

Without loss of generality, we can assume that $\vec{\lambda}$ points along the positive direction on the z-axis. In this case the scalar product of $\vec{\Omega}$ and $\vec{\lambda}$ is $\vec{\Omega} \cdot \vec{\lambda} = \cos \theta = \mu$. Using the normalization for the angular integration of Eq. (2.65) introduced in section 2.5,

$$\int d\Omega = \int_0^\pi \frac{d\mu}{2} \int_0^{2\pi} \frac{d\varphi}{2\pi} \quad (3.19)$$

one can easily see that the complex part of integral in Eq. (3.18) is zero since the integrand is an odd function integrated over symmetric limits. The real part of Eq. (3.18) is evaluated to

$$\omega(\vec{\lambda}) = \frac{\sigma_s}{\sigma} \int_{-1}^1 \frac{d\mu/2}{1 + (a\mu)^2} = \frac{\sigma_s}{\sigma} \cdot \frac{\tan^{-1} a}{a}, \quad (3.20)$$

where $a = |\vec{\lambda}|/\sigma$. The value of a that maximizes $|\omega(\vec{\lambda})|$ in Eq. (3.20) is equal to $a = 0$. As a result, the spectral radius for the isotropic problem using a fixed source iteration scheme is,

$$\rho \equiv \sup_{\vec{\lambda}} |\omega(\vec{\lambda})| = \frac{\sigma_s}{\sigma}, \quad (3.21)$$

which is a well-known result (Larsen E W, 2010; Valougeorgis et al., 1988).

Now we add a bit of complexity to our problem and consider the case of anisotropic scattering. We begin by expanding the group-to-group differential scattering cross section in Eq. (3.1) in Legendre polynomials,

$$\sigma_{s,gg'}(\vec{\Omega} \cdot \vec{\Omega}') = \sum_{l=0}^{\infty} (2l+1) \sigma_{l,gg'} P_l(\vec{\Omega} \cdot \vec{\Omega}'). \quad (3.22)$$

where the Legendre coefficients in Eq. (3.22) are defined as

$$\sigma_{l,gg'} = \int_{-1}^1 \sigma_{s,gg'}(\vec{\Omega} \cdot \vec{\Omega}') P_l(\vec{\Omega} \cdot \vec{\Omega}') \frac{d(\vec{\Omega} \cdot \vec{\Omega}')}{2}. \quad (3.23)$$

with the orthogonality condition for Legendre polynomials

$$\int_{-1}^1 P_l(\mu) P_{l'}(\mu) d\mu = \frac{2}{2l+1} \delta_{ll'}. \quad (3.24)$$

Using this information, we can simplify the transport Eq. (3.1) for anisotropic scattering if we perform the integration over the Ω' variable. First we decouple $\vec{\Omega}$ and $\vec{\Omega}'$ variables in Eq. (3.23) using the relation between Legendre polynomials and spherical harmonics,

$$P_l(\vec{\Omega} \cdot \vec{\Omega}') = \frac{1}{2l+1} \sum_{m=-l}^l Y_{lm}^*(\vec{\Omega}) Y_{lm}(\vec{\Omega}'). \quad (3.25)$$

Substituting Eq. (3.25) into Eq. (3.22) transforms it to

$$\sigma_{s,gg'}(\vec{\Omega} \cdot \vec{\Omega}') = \sum_{l=0}^{\infty} \sum_{m=-l}^l \sigma_{l,gg'} Y_{lm}^*(\vec{\Omega}') Y_{lm}(\vec{\Omega}). \quad (3.26)$$

In addition, we expand the angular flux over the spherical harmonics basis,

$$\psi_g(\vec{r}, \vec{\Omega}) = \sum_{l=0}^{\infty} \sum_{m=-l}^l \phi_{lm,g}(\vec{r}) Y_{lm}(\vec{\Omega}), \quad (3.27)$$

where the angular flux moments $\phi_{lm,g}$ are found using orthogonality conditions for spherical harmonics

$$\int d\Omega Y_{lm}(\vec{\Omega}) Y_{l'm'}^*(\vec{\Omega}) = \delta_{ll'} \delta_{mm'}, \quad (3.28)$$

producing,

$$\phi_{lm,g}(\vec{r}) = \int \psi_g(\vec{r}, \vec{\Omega}) Y_{lm}^*(\vec{\Omega}) d\Omega. \quad (3.29)$$

Thus, with the definitions provided in Eqs. (3.26), (3.27) and using the orthogonality of Eq. (3.28), the iterative form of the transport Eq. (3.1) for anisotropic scattering potential becomes

$$\left[\vec{\Omega} \cdot \vec{\nabla}_r + \sigma_g \right] \psi_g^{(t+1)}(\vec{r}, \vec{\Omega}) = \sum_{lm} \sigma_{l,gg} \phi_{lm,g}^{(t)}(\vec{r}) Y_{lm}(\vec{\Omega}) + s_g(\vec{r}, \vec{\Omega}), \quad (3.30)$$

where the source $s_g(\vec{r}, \vec{\Omega})$ is defined by expression

$$s_g(\vec{r}, \vec{\Omega}) = \sum_{g' \neq g}^{N_G} \sum_{l=0}^{\infty} \sum_{m=-l}^l \sigma_{l,gg'} \phi_{lm,g'}(\vec{r}) + S_g(\vec{r}, \vec{\Omega}) \quad (3.31)$$

The second equation of iterative cycle, that accompanies Eq. (3.30) is

$$\phi_{lm,g}^{(t)}(\vec{r}) = \int d\Omega \psi_g^{(t-1)}(\vec{r}, \vec{\Omega}) Y_{lm}^*(\vec{\Omega}). \quad (3.32)$$

Similar to the isotropic case, we omit the index g for clarity, always assuming a particular energy group. The iterative differences and their Fourier expansions are

defined by Eqs. (3.7), (3.8) and Eqs. (3.11), (3.12) with minor modifications where the scalar flux is substituted by the angular flux moments: $\delta\phi \rightarrow \delta\phi_{lm}$. Reformulation of Eqs. (3.30), (3.32) in terms of $\delta\psi$ and $\delta\phi_{lm}$, and after Fourier mode decomposition, produces the following system of integro-algebraic equations,

$$\left[i\vec{\Omega} \cdot \vec{\lambda} + \sigma \right] a^{(t+1)}(\vec{\lambda}, \vec{\Omega}) = \sum_{l=0}^{\infty} \sum_{m=-l}^l \sigma_l b_{lm}^{(t)}(\vec{\lambda}) Y_{lm}(\vec{\Omega}), \quad (3.33)$$

$$b_{lm}^{(t)}(\vec{\lambda}) = \int d\Omega a^{(t)}(\vec{\lambda}, \vec{\Omega}) Y_{lm}^*(\vec{\Omega}). \quad (3.34)$$

As before, solving for $a^{(t)}$ from Eq. (3.34) and substituting into Eq. (3.33) results in an iterative problem of the form,

$$b_{lm}^{(t)}(\vec{\lambda}) = \sum_{l'=0}^{\infty} \sum_{m'=-l'}^{l'} \sigma_{l'} \int d\Omega \frac{Y_{lm}^*(\vec{\Omega}) Y_{l'm'}(\vec{\Omega})}{i\vec{\Omega} \cdot \vec{\lambda} + \sigma} b_{l'm'}^{(t-1)}(\vec{\lambda}). \quad (3.35)$$

Equation (3.35) can also be presented in operator form,

$$b^{(t+1)}(\vec{\lambda}) = \mathbf{T} b^{(t)}(\vec{\lambda}), \quad (3.36)$$

where the vector $b^{(t)}$ is defined by its components $b_{lm}^{(t)}(\vec{\lambda})$. Note, that (lm) is a vector multi-index and the matrix \mathbf{T} is defined by

$$T_{(lm)(l'm')} = \sigma_{l'} \int d\Omega \frac{Y_{lm}^*(\vec{\Omega}) Y_{l'm'}(\vec{\Omega})}{i\vec{\Omega} \cdot \vec{\lambda} + \sigma}. \quad (3.37)$$

It is the largest eigenvalue of \mathbf{T} in Eq. (3.37) that defines the convergence of the iterative solution. A closer look at Eq. (3.37) suggests further simplifications to the matrix \mathbf{T} can be performed by integration over the azimuthal variable φ due to

orthogonality of the spherical harmonics. Once again, without loss of generality, we choose our coordinate system such that the direction of $\vec{\lambda}$ and positive z-axis coincide. Then $\vec{\Omega} \cdot \vec{\lambda} = \lambda\mu$, where $\mu = \cos\theta$. The relation between spherical harmonics and associate Legendre polynomials is expressed by

$$Y_{lm}(\vec{\Omega}) = Y_{lm}(\mu, \varphi) = \sqrt{\frac{(2l+1)(l-m)!}{(l+m)!}} P_{lm}(\mu) e^{i\varphi m}. \quad (3.38)$$

Thus, integration over φ in Eq. (3.37), gives simpler representation of iteration matrix \mathbf{T} ,

$$T_{(lm)(l'm')} = \delta_{mm'} C_{ll'}^m \sigma_{l'} \int_{-1}^1 \frac{d\mu}{2} \frac{P_{lm}(\mu) P_{l'm}(\mu)}{i\lambda\mu + \sigma}. \quad (3.39)$$

The coefficients $C_{ll'}^m$ are defined by the formula

$$C_{ll'}^m = \sqrt{\frac{(2l+1)(l-m)!}{(l+m)!}} \sqrt{\frac{(2l'+1)(l'-m)!}{(l'+m)!}} \quad (3.40)$$

In practical calculations, summation over l always has a finite upper limit l_{max} . It is easy to verify that in the case of isotropic scattering where $l_{max} = 0$, Eq. (3.37) reduces to the isotropic result in Eq. (3.16).

As an example, Eq. (3.39) is used to analytically obtain the spectral radius for the simplest nontrivial anisotropy of $l_{max} = 1$. In this case, the iterative matrix \mathbf{T} is a 2×2 matrix, and the eigenvalues are easily extracted using the relation (Valougeorgis et al., 1988),

$$\omega_{1,2} = \frac{1}{2} \left[\text{Tr}(\mathbf{T}) \pm \sqrt{(\text{Tr}(\mathbf{T}))^2 - 4 \det \mathbf{T}} \right]. \quad (3.41)$$

After optimization over λ in a similar fashion as to what was performed for the isotropic scattering case, the spectral radius for this system is equal to that of the

isotropic system $\rho = \sigma_0/\sigma$.

For larger degrees of anisotropy ($l_{max} > 1$), exact formulas become excessively complex. Below we prove the same result for higher orders of anisotropy using a semi-numerical approach. For this reason, we slightly rearrange Eq. (3.39) in the following way,

$$T_{(lm)(l'm')} = \frac{1}{\sigma} \delta_{mm'} \sigma_{l'} \tilde{T}_{l'}^m, \quad (3.42)$$

where the structure of $\tilde{T}_{l'}^m$ is deduced from Eq. (3.39),

$$\tilde{T}_{l'}^m = C_{l'}^m \int_{-1}^1 \frac{d\mu}{2} \frac{P_{lm}(\mu) P_{l'm}(\mu)}{i\mu(\lambda/\sigma) + 1}. \quad (3.43)$$

The reason for pulling out the factor σ^{-1} will become clear soon.

Due to the restriction $m = m'$ that arose from the spherical harmonic orthogonality condition (Eq. 3.28), only few elements of \mathbf{T} are non-zero. After appropriate swapping of columns and rows and using the symmetry property $\tilde{T}_{l'}^{-m} = \tilde{T}_{l'}^m$, one obtains a block-diagonal matrix of the form,

$$T = \frac{1}{\sigma} \begin{pmatrix} [m=0] & 0 & \cdots & 0 \\ 0 & [m=1] & \cdots & 0 \\ \vdots & \vdots & \ddots & \vdots \\ 0 & 0 & \cdots & [m=l_{max}] \end{pmatrix} \quad (3.44)$$

Each block in this matrix contains elements with specific value m . Matrix indices

l and l' range from m to l_{max} . For example, the block with $m = 1$ looks as follows,

$$T_{l'}^{m=1} = \frac{1}{\sigma} \begin{bmatrix} \sigma_1 \tilde{T}_{11}^1 & \sigma_2 \tilde{T}_{12}^1 & \cdots & \sigma_{l_{max}} \tilde{T}_{1l_{max}}^1 \\ \sigma_1 \tilde{T}_{21}^1 & \sigma_2 \tilde{T}_{22}^1 & \cdots & \vdots \\ \vdots & \vdots & \ddots & \vdots \\ \sigma_1 \tilde{T}_{l_{max}1}^1 & \cdots & \cdots & \sigma_{l_{max}} \tilde{T}_{l_{max}l_{max}}^1 \end{bmatrix}. \quad (3.45)$$

The block-diagonal form of Eq. (3.44) simplifies the determination of the spectral radius since the optimization of the largest eigenvalue is performed separately for each block. We performed these optimizations in Wolfram Mathematica 10. Our numerical simulations reveal that the largest eigenvalue for each block is evaluated to

$$\omega_m = \sigma_{l'=m} / \sigma. \quad (3.46)$$

Therefore, the spectral radius for the system is equal to the highest value of $\sigma_{l'=m} / \sigma$. For physical problems the isotropic differential cross section σ_0 is the largest one in the Legendre expansion. This proves that the convergence of anisotropic non-magnetic systems is the same as that of the isotropic case and is equal to $\rho = \sigma_0 / \sigma$.

3.2 Continuous LBTE with Magnetic Fields

One of the first works that incorporated the magnetic field into LBTE was published by St-Aubin et al. (2015, 2016). We restate this equation here for convenience in the

energy multigroup approximation (section **2.1**),

$$\left[\vec{\Omega} \cdot \vec{\nabla}_r + \kappa_g \vec{\tau}(\vec{\Omega}, \vec{B}) \cdot \vec{\nabla}_\Omega + \sigma_g \right] \psi_g(\vec{r}, \vec{\Omega}) - \sum_{g'=1}^{N_G} \int d\Omega' \sigma_{s,gg'}(\vec{\Omega} \cdot \vec{\Omega}') \psi_{g'}(\vec{r}, \vec{\Omega}') = S_g(\vec{r}, \vec{\Omega}). \quad (3.47)$$

The magnetic field term $\kappa_g \vec{\tau}(\vec{\Omega}, \vec{B}) \cdot \vec{\nabla}_\Omega$, with components defined by Eqs. (**2.29**, **2.30**, **2.62**), accounts for magnetic field effects for arbitrary magnetic field orientations. In infinite homogeneous medium the specific direction of the magnetic field is irrelevant. Thus, we assume an orientation of the magnetic field along the z-axis which simplifies the calculations significantly. Such a simplification allows us to obtain the expression of the spectral radius in an analytical form that is amenable for further analysis. For $\vec{B} = B\hat{z}$ magnetic field term simplifies to,

$$\kappa_g \vec{\tau}(\vec{\Omega}, \vec{B}) \cdot \vec{\nabla}_\Omega = \kappa_g B \frac{\partial}{\partial \varphi}. \quad (3.48)$$

Without loss of generality, we will again suppress the group index g in all subsequent equations, and consider a one group problem.

Since the energy discretization parameter κ and the magnetic field strength B always appear together, and their total combined magnitude is what affects the spectral radius, these parameters are investigated together. For brevity, in the discussion that follows, the combined parameters κB will be termed the *magnetic field parameter*.

As explained in section **2.5**, source iteration is implemented as a Gauss-Seidel iterative method for solving systems of linear equations. This technique leaves some degree of freedom to decide how to solve the magnetic field operator. We first explore

the possibility where magnetic field term is moved to the right side of Eq. (3.47) to be a part of an iterative source. The position of magnetic field term in iterative equation can affect the overall stability and convergence of iterative solution which in general depend on the parameters in the system. If the solution is convergent, the desired accuracy is achieved by appropriate number of iterations until the relative error falls below specified value. To ensure that the obtained solution is physically correct, the method should be tested against well known experiments, and/or against other dose calculation codes (e.g. Monte Carlo codes such as Geant4, EGSnrc, etc.).

To minimize the effort, we exploit the results obtained for the non-magnetic anisotropic case. The effect of the differential operator in Eq. (3.48) on the angular flux in Eq. (3.27) is

$$\kappa B \frac{\partial}{\partial \varphi} \psi(\vec{r}, \vec{\Omega}) = \sum_{l=0}^{\infty} \sum_{m=-l}^l im\kappa B \phi_{lm}(\vec{r}) Y_{lm}(\vec{\Omega}). \quad (3.49)$$

Combining Eq. (3.49) with the scattering term on the right side of Eq. (3.30) results in the following iterative equation,

$$\begin{aligned} \left[\vec{\Omega} \cdot \vec{\nabla}_r + \sigma \right] \psi^{(t+1)}(\vec{r}, \vec{\Omega}) = \\ \sum_{lm} (\sigma_l - im\kappa B) \phi_{lm}^{(t)}(\vec{r}) Y_{lm}(\vec{\Omega}) + s(\vec{r}, \vec{\Omega}). \end{aligned} \quad (3.50)$$

We note, that Eq. (3.50) can be obtained from Eq. (3.30) by formal substitution $\sigma_l \rightarrow (\sigma_l - im\kappa B)$. This allows us to immediately write down the expression for the iteration matrix \mathbf{T} , analogous to that of Eq. (3.39),

$$T_{(lm)(l'm')} = \delta_{mm'} C_{l'l}^m (\sigma_{l'} - im\kappa B) \int_{-1}^1 \frac{d\mu}{2} \frac{P_{lm}(\mu) P_{l'm}(\mu)}{i\lambda\mu + \sigma}. \quad (3.51)$$

Since the structure of the integrals in Eq. (3.39) and Eq. (3.51) are identical, we can right down the eigenvalue of each m -block $T_{ll'}^m$ with the largest absolute value in the form Eq. (3.46) by applying substitution $\sigma_l \rightarrow (\sigma_l - im\kappa B)$,

$$\omega_m = \frac{\sigma_{l'=m} - im\kappa B}{\sigma}. \quad (3.52)$$

An analysis of the eigenvalue expression in Eq. (3.52) clearly shows that, as the value of the magnetic field parameter grows in magnitude, the spectral radius can become larger than unity, which leads to divergence of the iterative scheme. It can also be seen from Eq. (3.52) that a higher degree of anisotropy (leading to a larger Legendre expansion order l_{max}) also makes the eigenvalues increase in magnitude and hampers the convergence when the spectral radius approaches unity, or leads to instability when it exceeds unity. Thus, treating the magnetic field term as a part of the iterative source leads to an unstable source iteration technique.

The behavior of spectral radius as a function of magnetic field parameter κB for $\sigma = 1.0 \text{ cm}^{-1}$ is shown in Fig. (3.1). Here we reinforce our results by estimating spectral radius according using the numerical approach of Eq. (2.55) from previously published work (St-Aubin et al., 2015). Figure (3.1) shows that Eq. (3.52) correctly reproduces the spectral radius dependence on magnetic field. The difference between analytical and numerical values shown in Fig. (3.1) is less than $10^{-4} \%$.

For low values of κB , the largest eigenvalue of iterative matrix is found for the $m = 0$ block. As the magnetic field parameter increases, the spectral radius remains constant until the largest eigenvalue from block $m = l_{max}$ becomes dominant. From that point, spectral radius becomes a linear function of κB and leads to divergence

for sufficiently large κB .

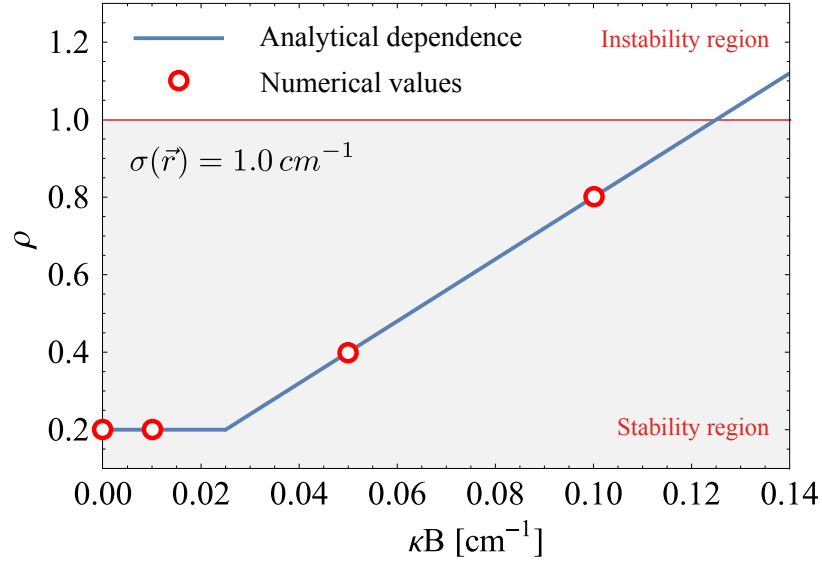


Figure 3.1: Spectral radius as a function of magnetic field parameter as predicted by Eq. (3.52) (solid line), and extracted numerically according to Eq. (2.55) using previously published code (St-Aubin et al., 2016).

We also consider the alternative situation where the magnetic field is treated as an operator (i.e. no iteration on the magnetic field term). In this case, the error form of LBTE for energy group g (index is omitted) looks as follows,

$$[\vec{\Omega} \cdot \vec{\nabla}_r + \kappa B \frac{\partial}{\partial \varphi} + \sigma] \delta \psi^{(t+1)}(\vec{r}, \vec{\Omega}) = \sum_{lm} \sigma_l \delta \phi_{lm}^{(t)}(\vec{r}) Y_{lm}(\vec{\Omega}), \quad (3.53)$$

$$\delta \phi_{lm}^{(t)}(\vec{r}) = \int d\Omega \delta \psi^{(t)}(\vec{r}, \vec{\Omega}) Y_{lm}^*(\vec{\Omega}). \quad (3.54)$$

To apply the Fourier analysis technique to Eqs. (3.53), (3.54), we use Eq. (3.11) in a slightly modified form adding to it a Fourier series expansion over the azimuthal

variable φ that is periodic on the sphere with period 2π ,

$$\delta\psi^{(t+1)}(\vec{r}, \vec{\Omega}) = \sum_{p=-\infty}^{\infty} \int d\vec{\lambda} a_p^{(t+1)}(\vec{\lambda}, \theta) e^{i\vec{\lambda}\vec{r}} e^{ip\varphi}. \quad (3.55)$$

Eqs. (3.55), (3.12) into Eq. (3.53) yields,

$$\sum_{p=-\infty}^{\infty} [i\vec{\Omega} \cdot \vec{\lambda} + i\kappa Bp + \sigma] a_p^{(t+1)}(\vec{\lambda}, \theta) e^{ip\varphi} = \sum_{lm} \sigma_l b_{lm}^{(t)}(\vec{\lambda}) Y_{lm}(\vec{\Omega}). \quad (3.56)$$

Equation (3.54) is transformed to the following,

$$b_{lm}^{(t)}(\vec{\lambda}) = \int d\Omega Y_{lm}^*(\vec{\Omega}) \sum_{m'=-\infty}^{\infty} a_{m'}^{(t)}(\vec{\lambda}, \theta) e^{im'\varphi} \quad (3.57)$$

In Eqs. (3.56), (3.57) we applied the previously used definition of Fourier modes independence and omitted the exponents $\exp(i\vec{\lambda}\vec{r})$ on both sides. To find the coefficients $a_p^{(t+1)}$ we multiply Eq. (3.56) by $\exp(im'\varphi)$ and integrate over $\int_0^{2\pi} d\varphi/(2\pi)$. Assuming the magnetic field is in z-direction and substituting $\vec{\Omega} \cdot \vec{\lambda} \rightarrow \lambda\mu$ we obtain,

$$[i\lambda\mu + i\kappa Bm' + \sigma] a_{m'}^{(t+1)}(\vec{\lambda}, \theta) = \sum_{l'=|m'|, |m'|+1, \dots} \sigma_{l'} b_{l'm'}^{(t)}(\vec{\lambda}) C_{l'm'} P_{l'm'}(\mu), \quad (3.58)$$

where the integration on the right side of Eq. (3.56) was performed using Eq. (3.38), and $C_{lm} = \sqrt{(2l+1)(l-m)!/(l+m)!}$.

Equation (3.58) is used to solve for $a_m^{(t+1)}$ from Eq. (3.57),

$$\begin{aligned}
b_{lm}^{(t)}(\vec{\lambda}) &= \int d\Omega Y_{lm}^*(\vec{\Omega}) \sum_{m'} a_{m'}^{(t)}(\vec{\lambda}, \theta) e^{im'\varphi} \\
&= \int_{-1}^1 \frac{d\mu}{2} \int_0^{2\pi} \frac{d\varphi}{2\pi} C_{lm} P_{lm}(\mu) e^{-im\varphi} \sum_{l'm'} \sigma_{l'} e^{im'\varphi} \frac{C_{l'm'} P_{l'm'}(\mu)}{i\lambda\mu + i\kappa Bm + \sigma} b_{l'm'}^{(t-1)}(\vec{\lambda}) \\
&= \sum_{l'} \sigma_{l'} \int_{-1}^1 \frac{d\mu}{2} \frac{C_{lm} P_{lm}(\mu) C_{l'm} P_{l'm}(\mu)}{i\lambda\mu + i\kappa Bm + \sigma} b_{l'm}^{(t-1)}(\vec{\lambda}), \tag{3.59}
\end{aligned}$$

or, in matrix form

$$b_{lm}^{(t)}(\vec{\lambda}) = T_{ll'} b_{l'm}^{(t-1)}(\vec{\lambda}), \tag{3.60}$$

with matrix $T_{ll'}$ defined by

$$T_{ll'} = \sigma_{l'} C_{ll'}^m \int_{-1}^1 \frac{d\mu}{2} \frac{P_{lm}(\mu) P_{l'm}(\mu)}{i\lambda\mu + i\kappa Bm + \sigma}. \tag{3.61}$$

The matrix in Eq. (3.61) is for a particular m value due to the block diagonal matrix form. We can make this equation even more general and write down Eq. (3.61) as follows,

$$T_{(lm)(l'm')} = \sigma_{l'} \int d\Omega \frac{Y_{lm}(\vec{\Omega}) Y_{l'm'}^*(\vec{\Omega})}{i\lambda\mu + i\kappa Bm' + \sigma}. \tag{3.62}$$

This form of the iteration matrix \mathbf{T} combines all the m -blocks and can be reduced to Eq. (3.61) after integration over azimuthal angle φ .

Analytical expressions for the largest eigenvalue of Eq. (3.61) for block m can be derived in principle, but will depend in a complex way on the magnetic field parameter κB , azimuthal number m , and maximum Legendre expansion order l_{max} . For simplicity, our investigations of Eq. (3.61) were performed numerically, and the

dependence of the eigenvalues on various strengths of magnetic field and azimuthal number m is shown in Fig. (3.2) for Legendre orders up to $l_{max} = 3$.

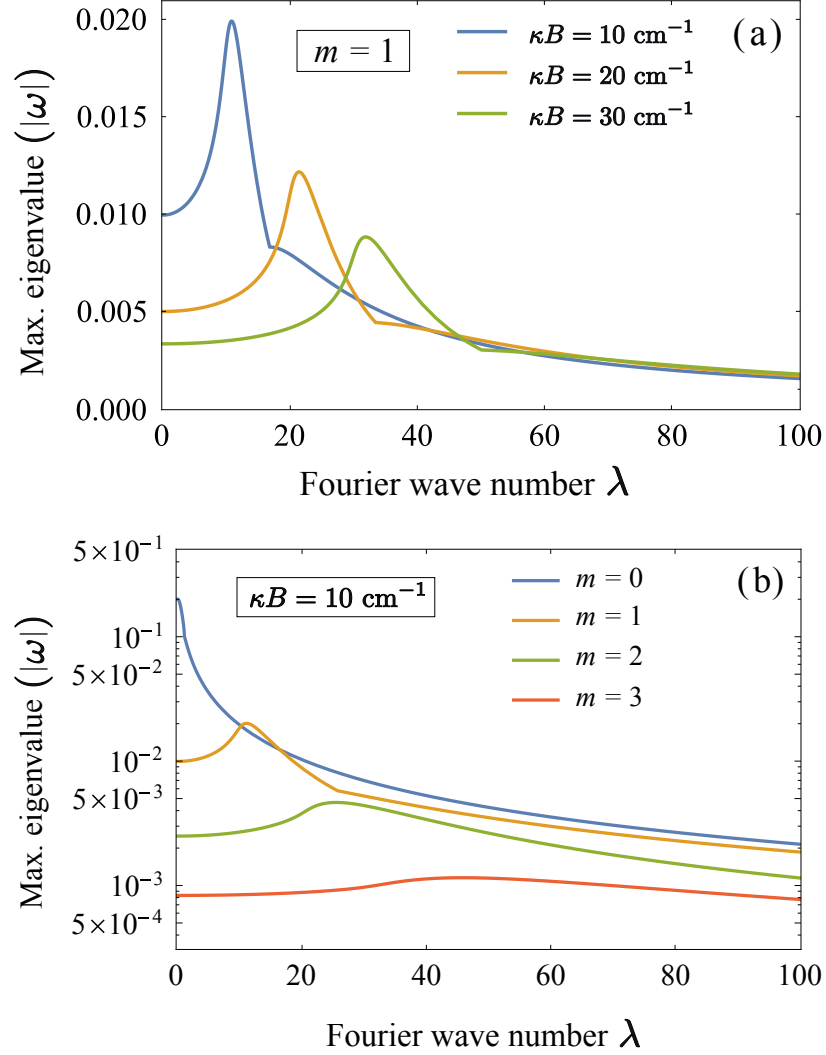


Figure 3.2: (a) Eigenvalue modulus ($|\omega|$) for various magnetic field parameter values inside $m = 1$ block of iteration matrix T in Eq. (3.62) as a function of the Fourier wave number λ , and (b) eigenvalue modulus as a function of the Fourier wave number λ and block number m for the fixed magnetic field parameter value $\kappa B = 10 \text{ cm}^{-1}$.

It should be noted that all the parameters that caused instability in the previous case, end up being in the denominator for this iterative scheme. Simulations show that

the spectral radius ρ of this source iteration scheme never exceeds unity regardless of the magnitude of the magnetic field parameter, or maximum Legendre expansion order. Figure **(3.2(a))** depicts the dependence of the largest eigenvalue in the $m = 1$ block on the magnitude of the magnetic field parameter. As the κB parameter increases, the maximal value of $|\omega_m(\lambda)|$ becomes progressively smaller. A similar behavior is observed in Fig. **(3.2(b))** where the degree of anisotropy is varied for a fixed magnetic field parameter. The tendency displayed is that for larger values of m , the peak of the function that described $|\omega_m(\lambda)|$ decreases. Based on these observations we conclude that the spectral radius is equal to the isotropic non-magnetic field case behavior in Eq. **(3.21)** (also seen in Fig. **3.2(b)** where the $m = 0$ eigenvalue is largest). This has the important results that the magnetic field has no impact on the spectral radius if treated as an operator, and that the iteration scheme is unconditionally stable.

Chapter 4

Spectral Radius of the Discretized Equations in Infinite Medium

In chapter **3** we performed a convergence analysis of the continuous LBTE with and without magnetic field in an infinite homogeneous medium. In this chapter, we intend to verify our findings and independently calculate spectral radius for the discretized transport equation where the angular and spatial domains are approximated by grids. The discrete form of transport equation is obtained using finite element analysis as described in section **2.6**.

We calculate the spectral radius numerically by obtaining the modulus of the largest eigenvalue of iterative matrix and independently by applying Eq. **(2.55)** using previously published code in (St-Aubin et al., 2016).

As seen previously, the spectral radius is a function of several parameters including magnetic field, material density, and anisotropy of scattering potential. The degree of

anisotropy dictates the maximum Legendre expansion order for accurate calculations. To account for these degrees of freedom in a systematic way we utilize the Henyey-Greenstein model (Ahrens, 2015; Henyey and Greenstein, 1941) for the differential scattering cross section $\sigma_s(\vec{\Omega} \cdot \vec{\Omega}')$, which takes the form

$$\sigma_s(\vec{\Omega} \cdot \vec{\Omega}') \equiv \sigma_s^{HG}(\nu) = \frac{\Lambda}{4\pi} \frac{1 - g^2}{(1 + g^2 - 2g\nu)^{3/2}}, \quad (4.1)$$

where $\nu = \cos \theta' = \vec{\Omega} \cdot \vec{\Omega}'$. The parameters in this formula are used to model anisotropy in a controllable way. The variable θ' is the polar coordinate denoting deviations from the forward direction, and the parameter g in the Heney-Greenstein model is a measure of the degree of anisotropy and varies in the limits $-1 \leq g \leq 1$. For $g = 1$ all the scattering processes tend to be in a forward direction (highest degree of anisotropy). When $g = 0$, the scattering is isotropic in nature. Negative values of g are used to model varying degrees of backscatter. Finally, the parameter Λ is used for normalization which is explained below.

In our simulations, we use two representative values for the anisotropy parameter g : $g = 0$ for isotropic scattering, and $g = 0.7$ that models forward-peaked anisotropic scattering (see Fig. 4.1) (Ahrens, 2015).

For these values of g the differential scattering cross section is expanded in Legendre polynomials,

$$\tilde{\sigma}_s^{HG}(\nu) = \sum_{l=0}^{l_{max}} (2l + 1) \sigma_l P_l(\nu) \quad (4.2)$$

with Legendre coefficients

$$\sigma_l = \frac{1}{2} \int_{-1}^1 P_l(\nu) \sigma_s^{HG}(\nu) d\nu. \quad (4.3)$$

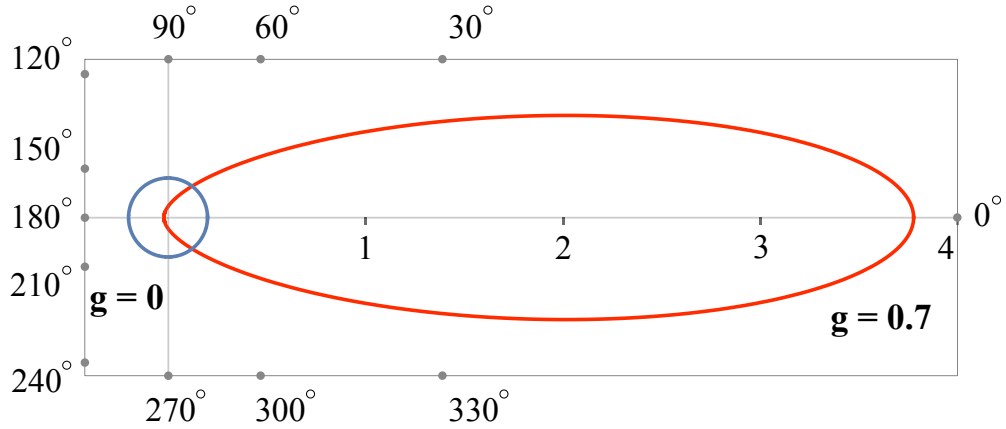


Figure 4.1: The Henyey-Greenstein function is used to model differential scattering cross section $\sigma_s(\vec{\Omega} \cdot \vec{\Omega}')$ for two values of anisotropy parameter $g = 0$ and 0.7 .

The value of the spectral radius depends crucially upon the accuracy of finite approximation using Eq. (4.2). A finite approximation of the differential cross section $\tilde{\sigma}_s^{HG}(\nu)$ given in Eq. (4.2) is achieved by terminating the series expansion at $l_{max} = 28$. This limit of expansion gives a relative error of 0.01% estimated according to,

$$\% = 100 \cdot \frac{\sqrt{\int_{-1}^1 [\sigma_s^{HG}(\nu) - \tilde{\sigma}_s^{HG}(\nu)]^2 d\nu}}{\sqrt{\int_{-1}^1 [\sigma_s^{HG}(\nu)]^2 d\nu}}. \quad (4.4)$$

The effect of the density of material on the convergence in the presence of magnetic fields is analyzed by allowing the total cross section σ to acquire several values in a wide range. As with anisotropy, we choose representative values for total cross section to be $\sigma = 10^{-3}, 10^0, 10^3 \text{ cm}^{-1}$. Another important parameter in our simulations is the ratio of the isotropic Legendre coefficient to the total cross section (not to be confused with the speed of light in Eq. (2.62))

$$c = \frac{\sigma_0}{\sigma} \quad (4.5)$$

The physical meaning of this ratio is that, regardless of the density of material, it shows how fast secondary electrons at energy E leave their energy group or exit the system (Lewis and Miller, 1993). For high values of c , significant numbers of particles enter the phase volume with the same energy E as other particles leave it due to scattering. This means that many collisions (and iterations for stationary methods) are required for convergence. This happens, for example, when secondary particles at energy E predominantly experience elastic scattering. On the other hand, if the ratio c is small, then particles quickly lose energy (or acquire energy, if up-scattering is present), which makes convergence fast. Thus, we test the dependence of the spectral radius on the magnetic field for three values of c -ratio, 0.2, 0.8, and 0.99. The last value is very close to unity where we expect poor convergence for the traditional source iteration approach.

The value of the isotropic Legendre coefficient σ_0 is derived in general from Eq.(4.3) for $l = 0$. However, it is also independently defined as the product $\sigma_0 = c\sigma$. Therefore, the normalization parameter Λ is adjusted to make both values equal. Hence,

$$\Lambda = 4\pi c\sigma. \quad (4.6)$$

In section 2.6 we applied a discontinuous finite element method in angle and space to obtain a discretized form of the LBTE with magnetic field (see Eqs. 2.122–2.128). For the DFEM in angle, the unit sphere with angular variable $\vec{\Omega}$ is tessellated into triangles and unwrapped onto a 2-D grid (St-Aubin et al., 2016). As was mentioned before, the angular grid is composed of 40 angular elements (section 2.6, Fig. 2.7). The solution inside the angular finite element is a subject to the boundary conditions in Eq. (2.130).

For arbitrary magnetic field orientations, DFEM discretization and the sweeping methodology for upwind stabilization (Lewis and Miller, 1993) can create complex cyclic sweep conditions (St-Aubin et al., 2016). However, by performing a coordinate transformation requiring the magnetic field to be situated along the z axis as in Eq. (3.48), only a single cyclic sweep condition is obtained at the $\varphi = 0$ boundary (St-Aubin et al., 2016) as shown in Fig. 13. The red shaded elements on the left-hand border $\varphi = 0$ are solved first, followed by the yellow shaded elements. The sweeping procedure continues up to the $\varphi = 2\pi$ border according to the blue arrows in Fig. (4.2). At the end of an iteration cycle, the value of the outgoing angular flux at the 2π border is assigned as the incoming angular flux at the $\varphi = 0$ boundary. That is, for iteration $(t + 1)$,

$$\psi_{inc}^{(t+1)}(\theta, \varphi = 0) = \psi^{(t)}(\theta, \varphi = 2\pi). \quad (4.7)$$

In discretizing the spatial domain, we followed the method outlined by Warsa et al. (2004) and explained in section 2.6. For spatial variables, the main domain is a cube which is subdivided into six tetrahedrons of equal volume (Fig. 4.3) which make up the spatial finite element domain discretization. As explained previously, such a partitioning contains the minimal number of FEM tetrahedral volume elements to simulate an infinite medium through a periodic repetition of the voxel with tetrahedral element faces aligning between the element in the original voxel and the element in the repeated voxel (Fig. 4.3). Inside a spatial voxel the solution obeys the boundary conditions expressed by Eq. (2.129).

For this work, we investigate an isotropic voxel which forms regular tetrahedrons, and a rectangular voxel with aspect ratio of 8:1:1. The latter rectangular voxel forms

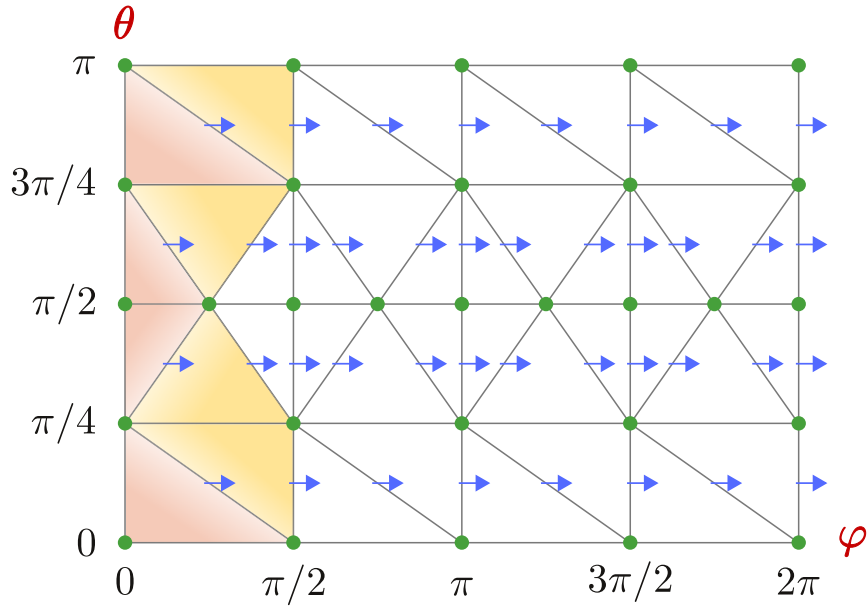


Figure 4.2: Angular finite element mesh showing the direction of the magnetic field operator \vec{r} and sweeping direction (arrows).

skewed tetrahedrons, and allows for the analysis on the spectral radius in this situation. Delaunay triangulation tries to limit the skewness of FEM tetrahedrons, but based on geometry there will always be some non-regular tetrahedrons in a practical FEM calculation.

Fourier analysis of the iterative convergence assumes a solution of the form Eq. (2.51),

$$\delta\psi(\vec{r}, \vec{\Omega}) \sim a(\vec{\lambda}) e^{i\vec{\lambda}\vec{r}}. \quad (4.8)$$

The solution for spatial elements with faces on the domain boundary (i.e. external surfaces) is defined using periodic boundary conditions. Figure (4.3) depicts two voxels, the main domain (solid lines) and a fictitious repeated domain which is created by the application of periodic boundary conditions (dashed lines). In Fig. (4.3), the points A and A' lie on corresponding surfaces obtained by a periodic translation.

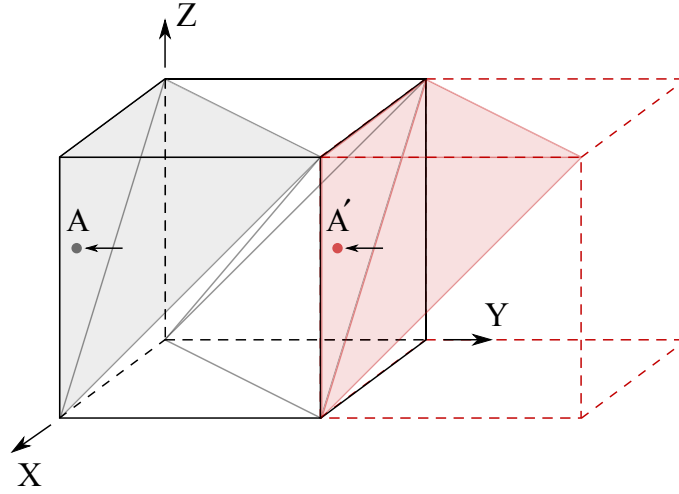


Figure 4.3: Spatial domain (cube) partitioned into six tetrahedrons. The main domain (solid lines) is periodically translated (dashed lines) to simulate an infinite medium.

The arrows indicate that the values of the solution on the surface are obtained by approaching A and A' from inside the elements. The boundary values at these points are related as

$$\delta\psi(\vec{r}_{A'}, \vec{\Omega}) = \delta\psi(\vec{r}_A, \vec{\Omega}) e^{i\lambda_x \Delta X}, \quad (4.9)$$

where λ_x is the x-component of Fourier wave number, and ΔX is the period of the main domain in x-direction. The same approach is used for the y- and z-directions. For the discretized problem, the solution is defined only at the nodes (corners) of the elements and the above boundary condition should be applied to every vertex of every element with a surface corresponding to an external surface on the domain.

The numerical simulations, from the setup of the linear systems, to the maximization of the eigenvalues of the iterative matrix over the Fourier wave number $\vec{\lambda}$, were performed using Wolfram Mathematica 10.

The Galerkin discontinuous FEM space-angle method converts the continuous

integro-differential linear Boltzmann transport Eqs. (2.97), (2.98) into a system of linear algebraic Eqs. (2.122–2.128) with boundary conditions in Eq. (2.129), (2.130). This system of equations can be compactly expressed using matrix operator form involving the angular flux and the angular flux moments errors $\delta\psi$ and $\delta\phi$ respectively in the Fourier Analysis,

$$\mathbf{L} \delta\psi^{(t+1)} = \mathbf{M}\Sigma \delta\phi^{(t)}. \quad (4.10)$$

The 1D vector $\delta\psi^{(t+1)} = \psi - \psi^{(t+1)}$ has its components are defined on every vertex in every element in the spatial and angular grids. Similarly, $\delta\phi^{(t)} = \phi - \phi^{(t)}$ is a 1D vector of angular flux moments $\delta\phi_{lm}^{(t)}$ defined on every vertex in every element of the spatial grid. The operator \mathbf{L} represents the combined action of discretized spatial streaming, collision, and angular streaming operators,

$$[\vec{\Omega} \cdot \vec{\nabla}_r + \vec{r}(\vec{\Omega}, \vec{B}) \cdot \vec{\nabla}_\Omega + \sigma] \Rightarrow \mathbf{L}. \quad (4.11)$$

The diagonal matrix Σ has on its diagonal the Legendre coefficients of the macroscopic differential electron scattering cross section σ_l ,

$$\Sigma = \text{diag}(\sigma_0, \sigma_1, \dots, \sigma_{l_{max}}). \quad (4.12)$$

Generally, the moment-to-discrete operator \mathbf{M} represents the discretized version of the expansion of the angular flux over the basis of spherical harmonics $Y_{lm}(\vec{\Omega})$,

$$\psi(\vec{r}, \vec{\Omega}) = \sum_{l=0}^{l_{max}} \sum_{m=-l}^l \phi_{lm}(\vec{r}) Y_{lm}(\vec{\Omega}) \Rightarrow \psi \approx \mathbf{M}\phi. \quad (4.13)$$

It can also be formally viewed as a mapping of the vector of an angular flux

moments ϕ_{lm} onto the vector of angular flux ψ . But, as noted in (Warsa et al., 2004), $\psi \neq \mathbf{M}\phi$, mainly due to the truncation of the Legendre expansion. The iterative expression in Eq. (4.10) is complemented by the discrete-tomoment operator \mathbf{D} defined as

$$\phi_{lm}(\vec{r}) = \int d\Omega \psi(\vec{r}, \vec{\Omega}) Y_{lm}^*(\vec{\Omega}) \Rightarrow \phi = \mathbf{D}\psi. \quad (4.14)$$

Equations (4.13), (4.14) between ψ and ϕ can help express the iterative Eq. (4.10) purely in terms of the angular flux vector errors $\delta\psi$, or the vector of angular flux moment errors $\delta\phi$. In the DFEM discretization of the LBTE with magnetic fields, the angular boundary conditions are applied (Eqs. 2.130, 4.7 and Fig. 4.2). This requires the iterative problem to be formulated in terms of angular flux, and not angular flux moments since the boundary conditions are in terms of the angular flux.

Below we describe the non-trivial dependence of the iterative scheme to solve Eq. (4.10) on the magnetic field, even though the magnetic field term is treated as a part of the streaming-collision operator. The sweeping requirement to update the angular flux at the boundary $\varphi = 0$ from the previous iteration changes the source iteration procedure. The flow of the angular flux (shown with arrows in Fig. 4.2) is determined by the vector $\vec{\tau}(\vec{\Omega}, \vec{B})$ which, with our choice for magnetic field in Eq. (3.48), is in the azimuthal direction $\hat{\varphi}$. For an interior finite element, boundary conditions in Eq. (2.130) are applied such that $\psi = \psi^{inc}$ at edges that meet the condition $\vec{\tau}(\vec{\Omega}, \vec{B}) \cdot \vec{n}_\alpha < 0$, where ψ^{inc} is the solution flowing from the upstream element and \vec{n}_α is the outward normal to the edge α of angular element. However, to begin the next iteration ($t+1$), the solution for the nodes at $\varphi = 0$ is provided by the angular flux at $\varphi = 2\pi$ from the previous (t)-th iteration. Thus, the application of the periodic boundary condition (PBC) is equivalent to part of magnetic field operator

acting as an iterative source. As was shown previously, when the magnetic field is part of the iterative source there is a detrimental impact on the spectral radius.

We model this adapted iterative procedure in our DFEM simulation by treating the part of matrix \mathbf{L} in Eq. (4.10) that is responsible for angular periodic boundary conditions as an iterative source,

$$\tilde{\mathbf{L}} \delta\psi^{(t+1)} = \mathbf{M}\Sigma\mathbf{D} \delta\psi^{(t)} - \mathbf{L}_{PBC} \delta\psi^{(t)}, \quad (4.15)$$

where $\tilde{\mathbf{L}} = \mathbf{L} - \mathbf{L}_{PBC}$.

Next, we rewrite Eq. (4.15) in the form

$$\delta\psi^{(t+1)} = \tilde{\mathbf{L}}^{-1}(\mathbf{M}\Sigma\mathbf{D} - \mathbf{L}_{PBC})\delta\psi^{(t)} = \mathbf{T} \delta\psi^{(t)}. \quad (4.16)$$

The spectral radius is obtained by finding the modulus of the largest eigenvalue of the iteration matrix \mathbf{T} obtained upon discretization of LBTE in space and angle using DFEM,

$$\mathbf{T} = \tilde{\mathbf{L}}^{-1}(\mathbf{M}\Sigma\mathbf{D} - \mathbf{L}_{PBC}). \quad (4.17)$$

Figure (4.4) displays the effect of the magnetic field parameter on the spectral radius for various medium densities for a scattering ratio of $c = 0.2$ for the isotropic spatial voxel (regular tetrahedrons). As seen in Fig. (4.4), there is very good agreement between the spectral radius calculated via Fourier analysis for the DFEM discretized equation and that estimated by the code from previously published work (St-Aubin et al., 2016).

From Fig. (4.4), it is clear that the DFEM sweeping approach (which makes the

\mathbf{L}_{PBC} operator part of the iterative source on the right side of the equation) increases the spectral radius.

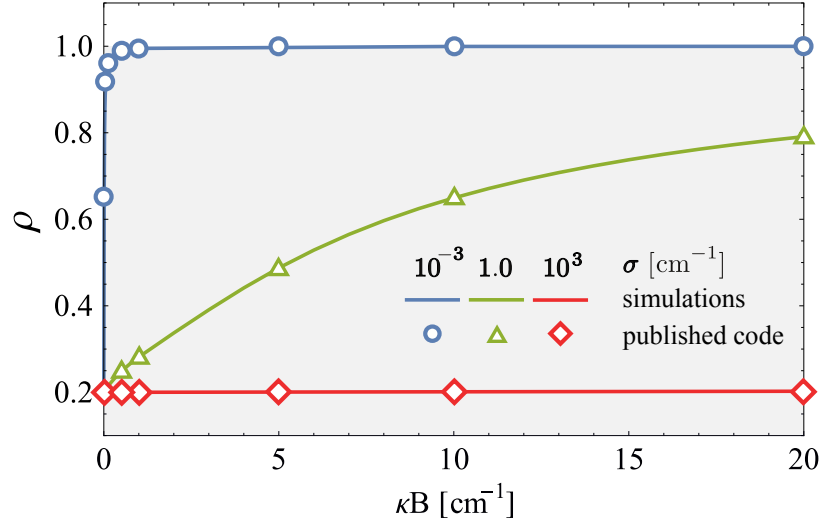


Figure 4.4: Spectral radius as a function of the magnetic field parameter for several medium densities with $c = 0.2$. Details of implementation of published code can be found in (St-Aubin et al., 2016).

The magnetic field parameter clearly has a dominant effect on the spectral radius in low density medium $\sigma = 10^{-3} \text{ cm}^{-1}$. Thus, the DFEM sweeping approach to solve the LBTE with magnetic fields worsens the spectral radius. The value of the spectral radius becomes sufficiently close to unity, even for relatively small magnetic field parameters, to make the source iteration approach impractical. It should be noted that despite the worsening of the spectral radius, and the inefficiency of source iteration, this scheme remains stable regardless of the strength of magnetic field (that is, the spectral radius monotonically approaches unity with the increasing strength of magnetic field). At the same time, the spectral radius for high density material ($\sigma = 10^3 \text{ cm}^{-1}$) is virtually unaffected by an increasing magnetic field parameter. This is thought to be due to the high density of scattering centers producing frequent

collisions and reducing the effect of the magnetic field. Materials with intermediate densities ($\sigma = 1.0 \text{ cm}^{-1}$) are partially affected by magnetic field with the spectral radius approaching unity at larger magnetic field parameter values. We note that by artificially keeping the operator \mathbf{L}_{PBC} on the left side of Eq. (4.15), this equation reduces to the same iterative scheme investigated for the continuous LBTE, and shows no dependence of the spectral radius on magnetic field as previously predicted in chapter 3.

The other values of parameter $c = 0.8, 0.99$ (not shown here) shift the zero magnetic field spectral radius towards unity. For these cases of high scattering ratios, the magnetic field increases the spectral radius in a similar fashion as shown in Fig. (4.4), with the exception that the spectral radius values simply start at the set scattering ratio (e.g. 0.8 or 0.99). Overall, for low density media with magnetic fields, or for media with scattering ratios close to unity the convergence rate of source iteration may be slow and other methods must be employed.

In addition, it was found that the spectral radius calculated with the high aspect ratio voxels (8:1:1) differed from the isotropic voxel by at most 0.04%. Thus, the aspect ratio (up to 8:1:1) of the spatial tetrahedrons has negligible impact on the spectral radius of the source iteration procedure.

Chapter 5

Improving the Convergence Rate via an Efficient Krylov-Subspace Solver

As was discussed in chapter 4, optically thick problems with a scattering ratio close to unity, and the discretized DFEM LBTE with magnetic fields in low density media, cause source iteration to become time consuming and inefficient. Non-stationary Krylov subspace methods for unsymmetrical matrices such as GMRES (Generalized Minimal Residual Method) (Saad, 1986) can efficiently handle a much broader class of matrix operators. GMRES has also been shown to accelerate the convergence rate of the standard LBTE in the past (Warsa et al., 2004). GMRES belongs to the family of Krylov subspace iterative numerical methods for solving large sparse systems of linear equations. In the absence of rounding errors, the convergence is guaranteed in no more than N steps, where N is the size of the matrix system. However, it has

been shown in practice that for many practical problems, GMRES converges in much less than the maximum N steps. However, due to the memory cost of storing all the Krylov basis, the modified version of the algorithm GMRES(m) is used in this work, where the iteration procedure to find the solution is restarted after $m = 20$ iterations.

To investigate the effectiveness of the restarted GMRES(m) to accelerate the LBTE with magnetic fields, we analyze its impact on isotropic and anisotropic scattering, and for sparse and dense media with both low and high scattering ratios.

As mentioned previously, a DFEM discretization of the LBTE results in a matrix equation $\mathbf{A}x = b$ with matrix operator \mathbf{A} being neither symmetric, nor positive definite. We can deduce the structure of the operator \mathbf{A} from the source iteration form of transport Eq. (4.16),

$$\psi^{(t+1)} = \tilde{\mathbf{L}}^{-1}(\mathbf{M}\Sigma\mathbf{D} - \mathbf{L}_{PBC})\psi^{(t)} + \tilde{\mathbf{L}}^{-1}S. \quad (5.1)$$

Here, we intend to find the angular flux ψ by directly solving the iterative Eq. (5.1) and operate in terms of the angular ψ (and not angular flux errors $\delta\psi$ which was required for the Fourier Analysis). The variable S in Eq. (5.1) denotes the discretized version of a source for this problem. The definition of other variables shown in Eq. (5.1) is the same as in the previous chapter 4.

By omitting the iterative superscripts, we define the matrix equation $\mathbf{A}x = b$ as,

$$\mathbf{A} = \mathbf{I} - \tilde{\mathbf{L}}^{-1}(\mathbf{M}\Sigma\mathbf{D} - \mathbf{L}_{PBC}), \quad (5.2)$$

and

$$b = \tilde{\mathbf{L}}^{-1}S. \quad (5.3)$$

Matrix \mathbf{I} in Eq. (5.2) is the identity matrix. In general, a rigorous quantification of the theoretical efficiency GMRES(m) is difficult. One qualitative approach, that allows to us make some conclusions about the convergence of the GMRES method, considers the spectrum of eigenvalues for matrix \mathbf{A} in Eq. (5.2) as well as its spectrum dynamics under the change of the system's parameters. It was observed by Warsa et al. (2004) that if the eigenvalues of the matrix \mathbf{A} cluster around the origin, it negatively affects the convergence. The inverse is also true: if the spectrum of \mathbf{A} is distributed away from the origin, it signifies faster convergence. We note, that the iteration processes for GMRES and SI are very different. The Krylov GMRES method requires more computational work per iteration cycle compared to SI, but the dramatic reduction in the number of iterations results in a decrease in the total calculational time (Warsa et al., 2004). Another important aspect of the GMRES solver is that the spectral radius is no longer an appropriate quantify to evaluate the efficiency of the method.

Figure (5.1) displays the eigenvalue spectrum of the matrix operator \mathbf{A} and its dynamics under increased magnetic field parameter values.

At zero magnetic field (Fig. 5.1(a)) the spectrum consists of two compact clusters around unity. This distribution of eigenvalues results in the fastest convergence in terms of iteration cycles. As the magnetic field parameter increases (Fig. 5.1(b,c)), there is pronounced drift of the eigenvalues towards the origin. For very large magnetic field parameters (Fig. 5.1(d)) the spectrum is again composed of two clusters, one of which is near the origin. Thus, in extreme cases of very high magnetic field

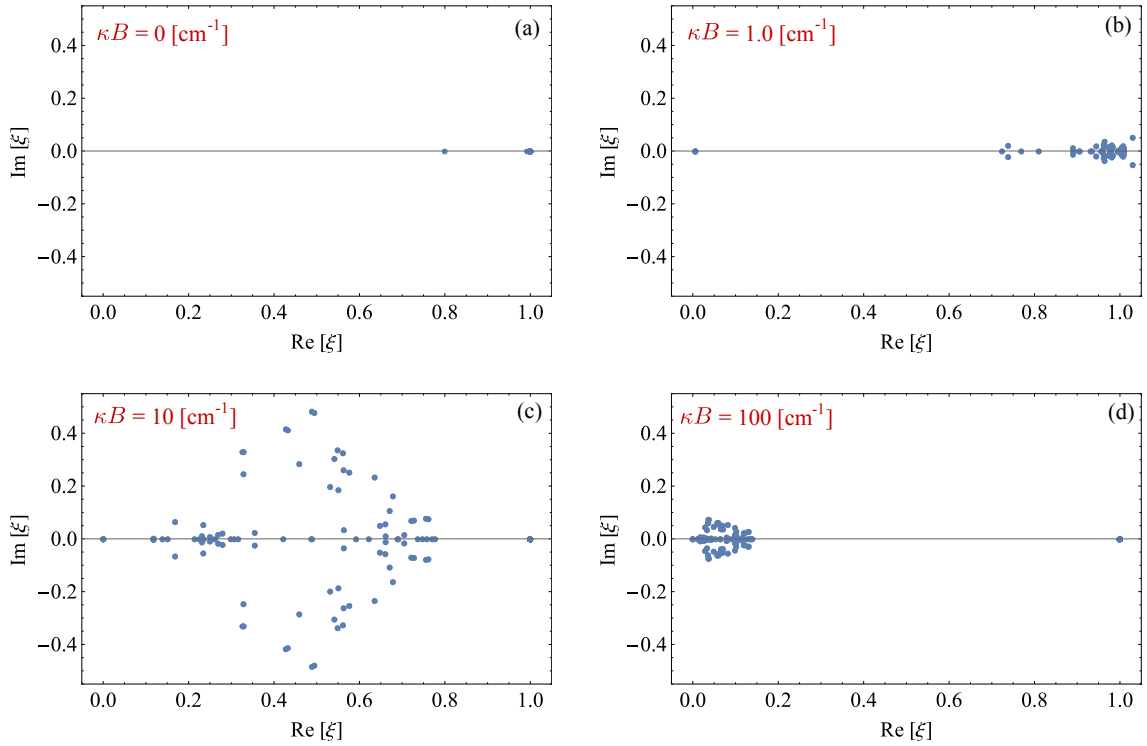


Figure 5.1: Eigenvalue spectrum of the matrix \mathbf{A} for various magnetic field parameter strengths. As the magnetic field parameter increases, the eigenvalues tend to cluster closer to zero, which is expected to have a negative impact on the convergence rate of GMRES.

parameters the presence of a significant portion of eigenvalues around the origin is expected to slow down the convergence rates of the GMRES(m) solver.

This discussion of effectiveness of GMRES in terms of dynamics of eigenvalues vs. magnetic field parameter is illustrative, but lacks the quantitative element. Thus, we also perform simulations in MATLAB 8.3 (The MathWorks Inc., Natick, MA, 2014) to compare the speed of convergence for GMRES versus source iteration based on the number of iterations required to achieve a desired accuracy dictated by the relative residual,

$$\epsilon = \frac{\|\psi^{(t+1)} - \psi^{(t)}\|}{\|\psi^{(t+1)}\|}. \quad (5.4)$$

In clinical scenarios the κB value depends on both the strength of magnetic field and energy via κ according to Eq. (2.62). In cases investigated here, $\kappa B = 10 \text{ cm}^{-1}$ corresponds approximately to a magnetic field strength of 20 T. This value is well beyond clinical MRI systems and was chosen to show the effectiveness of GMRES algorithm even in this extreme scenario.

Surprisingly, we found that even for much larger values of $\kappa B = 100 \text{ cm}^{-1}$ when a substantial number of the eigenvalues of \mathbf{A} cluster around the origin (Fig. 5.1(d)), the convergence of the solution to a relative error of 10^{-6} requires only five iterations for the system under consideration. This indicates a significant robustness of the GMRES method with respect to a wide range of magnetic field parameter values.

To complete the picture, we tested GMRES performance on the system with anisotropic scattering as well as an optically dense system with high scattering ratio. We found that inclusion of anisotropy for our system required only a few extra iterations. Similarly, increasing the scattering ratio c from 0.2 to 0.99 for dense medium requires less than 10 extra iterations.

This efficiency of the restarted GMRES solver is contrasted with that of the source iteration approach (Fig. 5.2(a,b)) for a material cross section value $\sigma = 10^{-3} \text{ cm}^{-1}$ where the magnetic field was shown to have a dominant impact on the spectral radius. Figure (5.2) shows that for $\kappa B = 10 \text{ cm}^{-1}$, the convergence of the source iteration solution for isotropic low density, low scattering ratio medium with material cross section $\sigma = 10^{-3} \text{ cm}^{-1}$ and $c = 0.2$ is four orders of magnitude slower than for GMRES and requires 12,380 iterations to converge to a relative error of 10^{-6} while GMRES(m) with a restart parameter of $m = 20$ required only 4 iterations (Fig. 5.2,

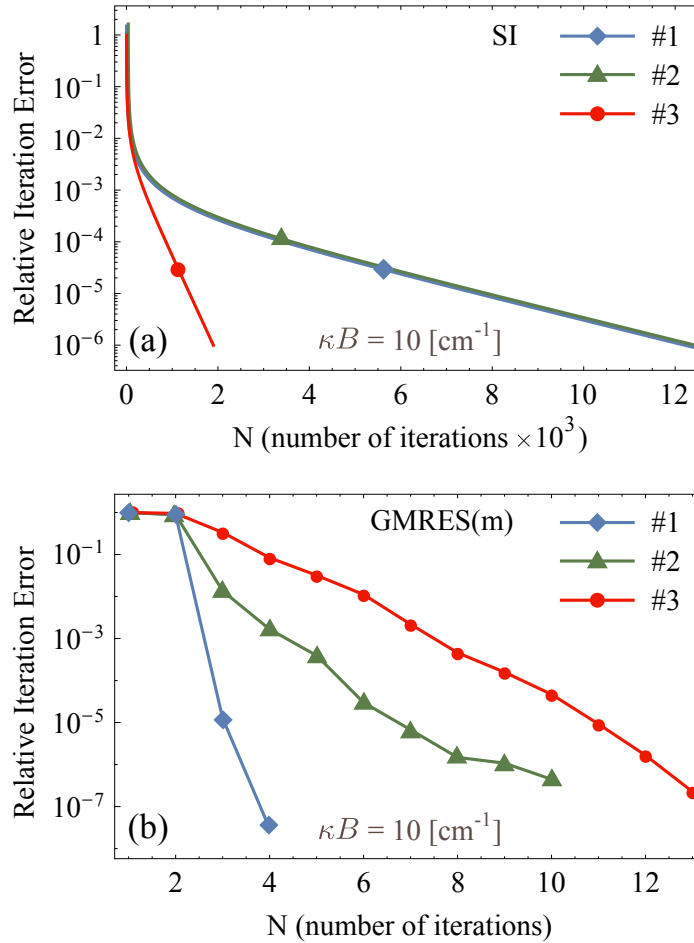


Figure 5.2: Comparison of the effectiveness of GMRES and SI iterative methods. [Curve #1: $g = 0$, $c = 0.2$, $\sigma = 10^{-3} \text{ cm}^{-1}$], [Curve #2: $g = 0.7$, $c = 0.2$, $\sigma = 10^{-3} \text{ cm}^{-1}$], [Curve #3: $g = 0.7$, $c = 0.99$, $\sigma = 10^3 \text{ cm}^{-1}$].

curve #1). The inclusion of anisotropy by setting $g = 0.7$ in the Heney-Greenstein model Eq. (4.1) increases the number of GMRES(m) iterations to 10, and number of iterations for source iteration up to 12,394 iterations (Fig. 5.2, curve #2). If, in addition, the cross section ratio is set close to unity ($c = 0.99$) for optically thick media $\sigma = 10^3 \text{ cm}^{-1}$, GMRES(m) converges after 13 iterations, but the number of source iterations drops to 1,901 iterations (Fig. 5.2, curve #3). Thus GMRES(m) is shown to effectively accelerate the convergence in all scenarios tested. It should be

noted that although the restarted version of GMRES with a restart number of 20 was used for this study, the number of GMRES iterations was below the restart number and thus never restarted. The choice of infinite homogeneous medium of low density material and high scattering ratio represent a worst case scenario. In practice, the angular flux is calculated inside the finite region. In this case, convergence is reached faster as many particles escape the region of interest.

Additionally, although this work has focused on homogeneous media for simplicity, a range of clinically relevant material cross sections were investigated representing a six order of magnitude variation from 10^{-3} to 10^3 . The convergence rate for an inhomogeneous medium (e.g. patient anatomy) is expected to be limited by the volume of material with the lowest cross section values.

Chapter 6

Conclusion and Future Work

Accuracy and speed of dose calculations are the cornerstones of any modern radiation treatment planning system. Started as “naïve” correction-based methodologies, dose calculation algorithms matured over time to advanced methods that account for fundamental physical processes of radiation interaction with matter. The dose calculation is based on the solution of linear Boltzmann transport equation where the dose is extracted from the analysis of radiation field as a function of space, time and energy variables (Eulerian approach employed by deterministic methods) or from the analysis of the histories of large number of particles propagating through the medium and interacting with its constituent atoms (Lagrangian approach via stochastic calculations used by Monte Carlo methods).

In this thesis we performed a rigorous iterative stability analysis of the novel deterministic dose calculation approach in magnetic fields published by St-Aubin et al. (2015, 2016). The effects of magnetic field, material density, energy, and anisotropy

expansion on the convergence were studied and some approaches for efficiency improvements were investigated.

The stability of the source iteration technique was performed using the Fourier analysis method. The analysis was done for the continuous LBTE with and without magnetic fields in an infinite homogeneous medium, and for the discretized version of LBTE with magnetic fields obtained using the discontinuous Galerkin finite element method.

For the continuous LBTE with magnetic fields, we extracted analytical expressions of the spectral radius for two source iteration models. The method which regards the magnetic field term as a part of the iteration source was determined to be iteratively unstable. The instability depended on the magnetic field strength, energy discretization, and degree of anisotropy. The second method investigated treated the magnetic field as part of the streaming-collision operator on the left side of the equation. The convergence of this model was found to be unconditionally stable (independent of the energy, magnetic field, or anisotropy expansion, l_{max}). In fact, for the continuous LBTE with magnetic fields, the magnetic field had no impact on the spectral radius whatsoever.

The numerical simulations of the discretized DFEM LBTE with magnetic fields required an alteration to the iterative scheme used in the continuous formalism to allow for upwind stabilization in angle as discussed in section **2.6**. In this altered iterative scheme, we confirmed the unconditional stability of the convergence for discretized LBTE seen in the continuous case. However, the spectral radius of the discretized DFEM equation possessed a non-trivial dependence on the magnetic field

parameter that was rooted in the numerical procedure employed for obtaining the solution. This dependence on magnetic field parameter was found to be important for low density materials as the spectral radius of the system quickly approached the unity even for weak magnetic fields parameter values resulting in a very poor convergence rate for the source iteration procedure.

To improve the convergence rate, we used an advanced GMRES solver that belongs to the class of nonstationary Krylov subspace methods that are known to be very robust when applied to iteration matrices with no symmetry. It was found that GMRES outperformed the source iteration method by orders of magnitude and demonstrated only a weak dependence on the magnetic field parameter.

In the future we would like to explore the possibility of using a different discretization method that would be completely unaffected by the magnetic field B . Our analytical analysis revealed unconditional stability and complete insensitivity of the spectral radius ρ to magnetic fields for the continuous LBTE when the magnetic field terms was treated completely as an operator. However, the upwind stabilized numerical solution obtained by applying the discontinuous Galerkin finite element method changed the iterative scheme and caused a dependence on the magnetic field parameter which increased the spectral radius. The poor convergence was caused by the numerical sweeping technique in angle which is a common stabilization method in DFEM for the first order equations to prevent unphysical and/or oscillatory solutions.

Thus, a potential solution to this is to investigate alternative stabilization strategies for the LBTE with magnetic fields such as a least square finite element method (LSFEM) and Streamline-Upwind/Petrov-Galerkin (SUPG) scheme. By going in

this direction, we hope to significantly reduce or completely suppress $\rho = \rho(B)$ dependence. That, in turn, can potentially allow us to apply standard acceleration techniques (such as diffusion synthetic acceleration) that are successfully used for non-magnetic systems to speed up the convergence (Warsa et al., 2004).

We also would like to propose a simple parallelization strategy for the angular domain. At the moment, our current results on this matter are incomplete. Therefore, below we only outline the general idea and leave the rigorous justification and testing of this method as a future work. Even though this discussion will focus on the parallelization in angular domain, with some modifications this approach can be applied to other variables.

In chapter **3** we observed that for nonzero magnetic fields, inclusion of the \mathbf{L}_{PBC} operator as an iterative source increases the spectral radius which increases the number of source iterations (chapter **4**, Fig. **5.2**). Parallelization in the angular domain introduces additional boundaries that will be included in the iterative source, and thus is expected to further negatively affect the convergence by further increasing the spectral radius and thus the total number of source iterations required. However, as was seen in chapter **4**, the non-stationary Krylov subspace method GMRES is relatively insensitive to an increasing magnetic field parameter. Thus, it is hypothesized that the use of GMRES as an iterative method would lessen the negative impact of parallelization where more boundaries are included in the \mathbf{L}_{PBC} operator. Clearly, a parallelization strategy is useful only if the negative effect of these additional boundaries is overpowered by the benefits of parallel calculations.

We begin by creating an angular discretization that can be broken into several

symmetric regions. An example with eight symmetric regions is shown in Fig. (6.1) (the grid itself is not shown). For each region, the red and blue colors denote entering and exiting fluxes respectively which in turn indicates the angular sweep direction defined by the direction of the $\vec{\tau}$ vector from Eq. (2.29). Since the angular flux in each region is calculated simultaneously, it would be expected that the total angular flux over the whole angular space would be calculated eight times faster for a linear parallelization speed up if no additional iterations were required. However, since additional iterations is expected be required due to the additional boundary terms in the iterative source, the effectiveness of the parallelization will be somewhat degraded.

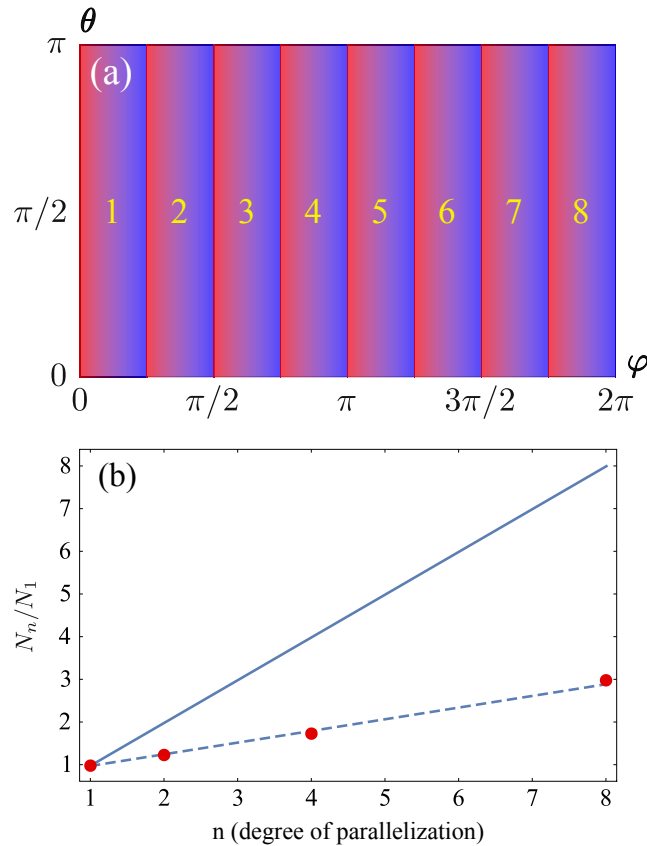


Figure 6.1: (a) Example of grid slab partitioning in the angular domain. Each slab is presumed to be solved in parallel independently, and (b) dependence of the relative number of GMRES iterations on the degree of parallelization.

If we let N_n be the total number of iterations required for a parallelization factor n , then in the case shown in Fig. **(6.1(a))** where there are eight regions ($n = 8$), effective parallelization would require the ratio N_8/N_1 to be less than eight (i.e. there is a less than eight times increase in the number of iterations). If the inequality $N_n/N_1 < n$ holds, parallelization is anticipated to be effective. The closer the ratio is to one the more effective the parallelization. The $N_n/N_1 = n$ case is denoted by solid line in Fig. **(6.1(b))**. Calculations were performed for parallelization factors of 2, 4 and 8, and are shown as the points in Fig. **(6.1(b))**.

Our simulations show that for this parallelization strategy, parallelization is effective, but is degraded slightly due to the increasing number of iterations required as more regions are parallelized. The true effectiveness of any parallelization strategy would have to be verified for a given implementation. However, these results show that there is a potential benefit to applying this parallelization strategy in addition to the application of GMRES(m) as the solver.

Bibliography

- M Abramowitz and I A Stegun. *Handbook of Mathematical Functions*. Dover Publications Inc., 1965.
- A Ahnesjö. Collapsed cone convolution of radiant energy for photon dose calculation in heterogeneous media. *Med. Phys.*, 16:577–92, 1989.
- A Ahnesjö and M M Aspradakis. Dose calculations for external photon beams in radiotherapy. *Phys. Med. Biol.*, 44:R99–R155, 1999.
- A Ahnesjö, P Andreo, and A Brahme. Calculation and application of point spread functions for treatment planning with high energy photon beams. *Acta Oncol.*, 26:49–56, 1987.
- C D Ahrens. Lagrange discrete ordinates: A new angular discretization for the three-dimensional linear boltzmann equation. *Nucl. Sci. Eng.*, 180:273–85, 2015.
- H F Batho. Lung corrections in cobalt 60 beam therapy. *J. Can. Assoc. Radiol.*, 15:79–83, 1964.
- A F Bielajew. The effect of strong longitudinal magnetic fields on dose deposition

- from electron and photon beams. *Med. Phys.*, 20:1171–9, 1993.
- J C Chai, H S Lee, and S V Patankar. Ray effect and false scattering in the discrete ordinates method. *Num. H. Tranf.*, 24(B):373–89, 1993.
- J R Clarkson. A note on depth doses in fields of irregular shape. *Br. J. Radiol.*, 14:265–68, 1941.
- J R Cunningham. Scatter-air ratios. *Phys. Med. Biol.*, 17:42–51, 1972.
- J F Dempsey, D Benoit, J R Fitzsimmons, A Haghghat, J G Li, D A Low, S Mutic, J R Palta, H E Romeijn, and G E Sjoden. A device for realtime 3d image-guided imrt. *Int. J. Radiat. Biol.*, 63:S202–S202, 2005.
- G A Failla, T Wareing, Y Archambault, and S Thompson. Acuros xb advanced dose calculation for the eclipse treatment planning system. Technical report, Varian Medical Systems, 2010.
- B G Fallone, B Murray, S Rathee, T Stanescu, S Steciw, S Vidakovic, E Blosser, and D Tymofichuk. First mr images obtained during megavoltage photon irradiation from a prototype integrated linac–mr system. *Med. Phys.*, 36:2084–8, 2009.
- M Fippel. Fast monte carlo dose calculation for photon beams based on the vmc electron algorithm. *Med. Phys.*, 26(8):1466–75, 1999.
- M Fippel. *Monte Carlo Techniques in Radiation Therapy*, chapter Basics of Monte Carlo Simulations, pages 17–28. CRC Press, 2013.
- K A Gifford, J L Horton, T A Wareing, G Failla, and F Mourtada. Comparison of a

- finite-element multigroup discrete-ordinates code with monte carlo for radiotherapy calculations. *Phys. Med. Biol.*, 51:2253–65, 2006.
- G H Golub and C F Van Loan. *Matrix Computations*. Johns Hopkins University Press), 2012.
- W Hackbusch. *Iterative Solution of Large Sparse Systems of Equations*. Springer, 2016.
- T Han, J K Mikell, M Salehpour, and F Mourtada. Dosimetric comparison of acuros xb deterministic radiation transport method with monte carlo and model-based convolution methods in heterogeneous media. *Med. Phys.*, 38(5):2651–64, 2011.
- L G Henyey and J L Greenstein. Diffuse radiation in the galaxy. *Astrophys. J.*, 93:70–83, 1941.
- F B Hildebrand. *Introduction to Numerical Analysis*. Dover Publications Inc., 1974.
- S Hissoiny, B Ozell, H Bouchard, and P Depres. Gpumcd: A new gpu-oriented monte carlo dose calculation platform. *Med. Phys.*, 38:754–764, 2011.
- E Isaacson and H B Keller. *Analysis of Numerical Methods*. Dover Publications, Inc., 1994.
- R Jeraj and P Keall. The effect of statistical uncertainty on inverse treatment planning based on monte carlo dose calculation. *Phys. Med. Biol.*, 45:3601–13, 2000.
- B Jiang. *The Least-Squares Finite Element Method*. Springer, 1998.

- J M Jin. *The Finite Element Method in Electromagnetics*. Wiley-EEE, 3rd ed. edition, 2014.
- A Keyvanloo, B Burke, J St-Aubin, D Baillie, K Wachowicz, B Warkentin, S Steciw, and B G Fallone. Minimal skin dose increase in longitudinal rotating biplanar linac-mr systems: examination of radiation energy and flattening filter design. *Phys. Med. Biol.*, 61:3527–39, 2016.
- F M Khan, S H Levitt, V C Moore, and T K Jr Jones. Computer and approximation methods of calculating depth dose in irregularly shaped fields. *Radiology*, 106:433–36, 1973.
- C Kirkby, B Murray, S Rathee, and B G Fallone. Lung dosimetry in a linac-mri radiotherapy unit with a longitudinal magnetic field. *Med. Phys.*, 37(9):4722–32, 2010.
- Morel J E Larsen E W. *Nuclear Computational Science. A Century in review*, chapter Advances in Discrete-Ordinates Methodology, pages 1–84. Springer, 2010.
- E E Lewis and W F Jr Miller. *Computational Methods of Neutron Transport*. American Nuclear Society, Inc., 1993.
- D Low, S Mutic, S Shvartsman, T Chmielewski, G Fought, A Sharma, and J Dempsey. Tu-h-bra-02: The physics of magnetic field isolation in a novel compact linear accelerator based mri-guided radiation therapy system. *Med. Phys.*, 43:3768, 2016.
- D A Low, W B Harms, S Mutic, and J A Purdy. A technique for the quantitative evaluation of dose distributions. *Med. Phys.*, 25:656–61, 1998.

- L Lu. Dose calculation algorithms in external beam photon radiation therapy. *Int. J. Cancer Ther. Oncol.*, 1(2):01025, 2013.
- T R Mackie, J W Scrimger, and J J Battista. A convolution method of calculating dose for 15-mv x rays. *Med. Phys.*, 12(2):188–96, 1985.
- J E Morel. Fokker-planck calculations using standard discrete ordinates transport codes. *Nucl. Sci. Eng.*, 79:340–56, 1981.
- J E Morel. Multigroup legendre coefficients for the diamond difference continuous slowing down operator. *Nucl. Sci. Eng.*, 91:324–31, 1985.
- U Oelkfe and C Scholz. *New Technologies in Radiation Oncology. Medical Radiology*, chapter Dose Calculation Algorithms, pages 187–96. Springer, 2006.
- N Papanikolaou. Tissue inhomogeneity corrections for megavoltage photon beams. Technical report, AAPM REPORT No. 85, 2004.
- A J E Raaijmakers, B W Raaymakers, and J J W Lagendijk. Integrating a mri scanner with a 6 mv radiotherapy accelerator: dose increase at tissue–air interfaces in a lateral magnetic field due to returning electrons. *Phys. Med. Biol.*, 50:1363–76, 2005.
- A J E Raaijmakers, B W Raaymakers, and J J W Lagendijk. Experimental verification of magnetic field dose effects for the mri-accelerator. *Phys. Med. Biol.*, 52:4283–91, 2007.
- B W Raaymakers, J J W Lagendijk, J Overweg, J G M Kok, A J E Raaijmakers, E M Kerkhof, R W van der Put, I Meijnsing, S P M Crijsns, F Benedosso, M van

- Vulpen, C H W de Graaff, J Allen, and K J Brown. Integrating a 1.5 t mri scanner with a 6 mv accelerator: proof of concept. *Phys. Med. Biol.*, 54:N229–N237, 2009.
- Y Saad. Gmres: A generalized minimum residual algorithm for solving nonsymmetric linear systems. *SIAM J. Sci. Stat. Comp.*, 7:856–69, 1986.
- D M Santos, J St-Aubin, B G Fallone, and S Steciw. Magnetic shielding investigation for a 6 mv in-line linac within the parallel configuration of a linac-mr system. *Med. Phys.*, 39(2):788–97, 2012.
- G Schoknecht. Description of radiation fields by separation of primary and scatter radiation. i. the tissue–air ratio in ^{60}Co fields. *Strahlentherapie*, 132:516–28, 1967.
- M R Sontag and J R Cunningham. The equivalent tissue-air ratio method for making absorbed dose calculations in a heterogeneous medium. *Radiology*, 129(3):787–94, 1978.
- J St-Aubin, S Steciw, and B G Fallone. Magnetic decoupling of the linac in a low field biplanar linac-mr system. *Med. Phys.*, 37(9):4755–61, 2010.
- J St-Aubin, A Keyvanloo, O Vassiliev, and B G Fallone. A deterministic solution of the first order linear boltzmann transport equation in the presence of external magnetic fields. *Med. Phys.*, 42:780–93, 2015.
- J St-Aubin, A Keyvanloo, and B G Fallone. Discontinuous finite element space-angle treatment of the first order linear boltzmann transport equation with magnetic fields: Application to mri-guided radiotherapy. *Med. Phys.*, 43:195–204, 2016.
- J Tertel, J Wulff, H Karle, and K Zink. Verification of a commercial implementa-

- tion of the macro-monte-carlo electron dose calculation algorithm using the virtual accelerator approach. *Z. Med. Phys.*, 20:51–60, 2010.
- D Valougeorgis, M Williams, and E W Larsen. Stability analysis of synthetic acceleration methods with anisotropic scattering. *Nucl. Sci. Eng.*, 99:91–8, 1988.
- O N Vassiliev, T A Wareing, J McGhee, G Failla, M R Salehpour, and F Mourtada. Validation of a new grid-based boltzmann equation solver for dose calculation in radiotherapy with photon beams. *Phys. Med. Biol.*, 55:581–98, 2010.
- J S Warsa, T A Wareing, and J E Morel. Krylov iterative methods and the degraded effectiveness of diffusion synthetic acceleration for multidimensional sn calculations in problems with material discontinuities. *Nucl. Sci. Eng.*, 147:218–48, 2004.
- H O Wooten, O Green, M Yang, T DeWees, R Kashani, J Olsen, J Michalski, D Yang, K Tanderup, Y Hu, H H Li, and S Mutic. Quality of intensity modulated radiation therapy treatment plans using a 60co magnetic resonance image guidance radiation therapy system. *Int. J. Radiation. Oncol. Biol. Phys.*, 92(4):771–8, 2015.
- T I Zohdi. *A Finite Element Primer for Beginners: The Basics*. Springer, 2014.